The Astrophysical Journal, 838:111 (17pp), 2017 April 1 https://doi.org/10.3847/1538-4357/aa6627

Triggering the Formation of Direct Collapse Black Holes by Their Congeners

Bin Yue (岳斌)[1,2], Andrea Ferrara[2,3], Fabio Pacucci[2,4], and Kazuyuki Omukai (大向一行)[5]
[1] National Astronomical Observatories, Chinese Academy of Sciences, Beijing, 100012, China; yuebin@bao.ac.cn
[2] Scuola Normale Superiore, Piazza dei Cavalieri 7, I-56126 Pisa, Italy
[3] Kavli IPMU (WPI), Todai Institutes for Advanced Study, University of Tokyo, Japan
[4] Department of Physics, Yale University, P.O. Box 208101, New Haven, CT 06520, USA
[5] Astronomical Institute, Tohoku University, Sendai, Miyagi 980-8578, Japan
Received 2016 December 22; revised 2017 March 6; accepted 2017 March 9; published 2017 March 31

Abstract

Direct collapse black holes (DCBHs) are excellent candidates for seeds of supermassive black holes observed at $z \gtrsim 6$. The formation of a DCBH requires a strong external radiation field to suppress H_2 formation and cooling in a collapsing gas cloud. Such a strong field is not easily achieved by first stars or normal star-forming galaxies. Here we investigate a scenario in which a previously formed DCBH can provide the necessary radiation field for the formation of additional ones. Using a one-zone model and simulated DCBH Spectral Energy Distributions (SEDs) filtered through absorbing gas initially having column density $N_{\rm H}$, we derive the critical field intensity, $J_{\rm LW}^{\rm crit}$, to suppress H_2 formation and cooling. For the SED model with $N_{\rm H} = 1.3 \times 10^{25}\,{\rm cm}^{-2}$, $8.0 \times 10^{24}\,{\rm cm}^{-2}$, and $5.0 \times 10^{24}\,{\rm cm}^{-2}$, we obtain $J_{\rm LW}^{\rm crit} \approx 22$, 35, and 54, all much smaller than the critical field intensity for normal star-forming galaxies $J_{\rm LW}^{\rm crit} \gtrsim 1000$. X-ray photons from previously formed DCBHs build up a high-z X-ray background (XRB) that may boost the $J_{\rm LW}^{\rm crit}$. However, we find that in the three SED models, $J_{\rm LW}^{\rm crit}$ only increases to ≈80, 170, and 390, even when $\dot{\rho}_\star$ reaches the maximum value allowed by the present-day XRB level (0.22, 0.034, $0.006\,M_\odot\,{\rm yr}^{-1}\,{\rm Mpc}^{-3}$), which is still much smaller than the galactic value. Although considering the XRB from first galaxies may further increase $J_{\rm LW}^{\rm crit}$, we conclude that our investigation supports a scenario in which DCBHs may be more abundant than predicted by models only including galaxies as external radiation sources.

Key words: dark ages, reionization, first stars – quasars: supermassive black holes – X-rays: diffuse background

1. Introduction

The quest for supermassive black holes (SMBHs) at $z \gtrsim 6$ has been a remarkable success (Fan et al. 2003; Jiang et al. 2007; Kurk et al. 2007; Mortlock et al. 2011; Morganson et al. 2012; Venemans et al. 2013; Wu et al. 2015). However, the detection of SMBHs as massive as $\sim 10^9$–$10^{10}\,M_\odot$ at such early epochs with cosmic age $\lesssim$1 Gyr has raised a number of questions that remain essentially unanswered.

Black holes (BHs) grow from an initial seed by accreting the surrounding gas. Naive SMBH seed candidates are stellar-mass BHs formed after the death of massive (possibly Pop III) stars, with a typical mass $\sim 100\,M_\odot$ or even smaller (Heger et al. 2003; Hosokawa et al. 2011). However, even assuming continuous accretion at the Eddington limit, the time required to grow a $\sim 10^9\,M_\odot$ SMBH by $z \sim 6$ is comparable to or even longer than the Hubble time at that redshift. Even worse, in the early evolutionary stages, radiative feedback reduces the accretion rate significantly. As a result, for most of the time, the BH grows slowly (Alvarez et al. 2009; Jeon et al. 2012; Valiante et al. 2016). Furthermore, reionization of the intergalactic medium (IGM) may also significantly hamper the growth process (Tanaka et al. 2012).

To overcome these problems, an alternative scenario in which an SMBH grows from a seed more massive than $10^4\,M_\odot$ has become popular (see, e.g., the review by Volonteri 2010). Such massive seeds are nicely produced by the so-called "direct collapse" process occurring in metal-free atomic-cooling halos with virial temperature $T_{\rm vir} \gtrsim 10^4$ K (Bromm & Loeb 2003; Koushiappas et al. 2004; Begelman et al. 2006, 2008; Lodato & Natarajan 2006; Regan & Haehnelt 2009; Begelman 2010; Agarwal et al. 2012, 2013, 2014, 2016b; Johnson et al. 2013; Latif et al. 2013a, 2013b, 2014, 2015, 2016; Latif & Ferrara 2016; Habouzit et al. 2016; Choi et al. 2015; Regan et al. 2014; Pacucci et al. 2015a, 2015b; Pacucci & Ferrara 2015). If in these halos H_2 formation and cooling are suppressed, metal-free gas can only cool via Lyα radiation, which becomes inefficient when the gas cools below ∼8000 K. Then, the gas contracts almost isothermally with $T \sim 8000$ K and avoids fragmentation during the cloud collapse (Inayoshi et al. 2014). Eventually, at the center, a BH with mass $\sim 10^4$–$10^6\,M_\odot$ forms (Ferrara et al. 2014). Thereafter, such a direct collapse black hole (DCBH) continues to accrete gas and may merge with other BHs. A fully fledged SMBH is then produced on timescales much shorter than the Hubble time.

The suppression of H_2 formation requires either a strong Lyman–Werner (LW; $11.2 < h\nu < 13.6$ eV) UV radiation field that directly dissociates H_2, or a strong continuum radiation field from the near-infrared (NIR) to the UV band ($0.755 < h\nu < 13.6$ eV) that detaches the most important H_2 formation catalyst, H^-. The required critical field intensity and the clustering of dark matter halos determine the actual abundance of DCBHs in the high-z universe (Dijkstra et al. 2008; Yue et al. 2014). The DCBH abundance has been studied by many authors, and the predicted number density at $z \sim 10$ ranges from $\sim 10^{-10}\,{\rm Mpc}^{-3}$ to $\sim 10^{-3}\,{\rm Mpc}^{-3}$ (e.g., Agarwal et al. 2012, 2013; Dijkstra et al. 2014; Visbal et al. 2014a; Pacucci et al. 2015a; Habouzit et al. 2016). Nevertheless, such a number density is much smaller than that of galaxies in the high-z universe.

Generally, in this scenario, the required critical field intensity is very high. For an ideal blackbody spectrum with effective temperature 10^4 K, $J_{\nu_{13.6}}^{\rm crit} \sim 30$–300 (Omukai 2001; Shang et al. 2010); for a realistic galaxy spectrum $J_{\nu_{13.6}}^{\rm crit} \gtrsim 1000$–10,000 (Sugimura et al. 2014; Latif et al. 2015), where $J_{\nu_{13.6}}$ is

the specific intensity of the radiation field at 13.6 eV and in units of 10^{-21} erg s^{-1} cm^{-2} Hz^{-1}sr^{-1}. Such a strong radiation field can be attained only when the radiation source is very close to the DCBH-forming gas cloud. In spite of this stringent requirement, the discovery of two high-z DCBH candidates in the CANDELS/GOODS-S survey has been recently reported (Pacucci et al. 2016). Moreover, the Lyman-alpha emitter (LAE) "CR7" has been observed and reported as a DCBH candidate by some authors, because Pop III stars can hardly provide its strong Lyα and He II 1640 Å line luminosities, and the two nearby Pop II galaxies are ideal sources for providing strong external radiation, although this detection is still a matter of debate (Pallottini et al. 2015; Sobral et al. 2015; Agarwal et al. 2016a; Bowler et al. 2016; Smidt et al. 2016; Smith et al. 2016; Pacucci et al. 2017).

In Yue et al. (2014), we proposed that an accreting and Compton-thick DCBH can provide a radiation field that suppresses H_2 formation in a more efficient way compared with a galaxy. The advantages here are, for the spectral energy distribution (SED) of a Compton-thick DCBH, the ratio of the H- photodetachment rate to the H_2 photodissociation rate (this ratio is the most straightforward indicator of the H_2 suppression efficiency, see Sugimura et al. 2014; Wolcott-Green et al. 2017) is higher than that for normal star-forming galaxies, and a BH is usually brighter than a galaxy. Moreover, there is an additional advantage: if the source also produces X-ray and ionizing photons, in general it may hamper DCBH formation (Inayoshi & Omukai 2011; Aykutalp et al. 2014; Johnson et al. 2014; Inayoshi & Tanaka 2015; Glover 2016; Regan et al. 2016); however, if the source is a Compton-thick DCBH, except for a few very hard X-ray photons (i.e., $\gtrsim$10 keV), for most of the accretion stage it does not emit X-rays and ionizing photons. In this case, the abundance of high-z DCBHs can be higher than currently expected.

In this work, we derive the critical field intensity for the formation of a new DCBH inside a collapsing gas cloud irradiated by a nearby previously formed DCBH using the one-zone model, in which the whole cloud is assumed to have uniform properties. The SEDs of the DCBH are taken from numerical simulations (Pacucci et al. 2015a). We consider three SED models with *initial* column number densities $N_{\rm H} = 1.3 \times 10^{25}\,{\rm cm}^{-2}$, $N_{\rm H} = 8.0 \times 10^{24}\,{\rm cm}^{-2}$, and $N_{\rm H} = 5.0 \times 10^{24}\,{\rm cm}^{-2}$. Throughout this paper, $N_{\rm H}$ refers to the column number density of the gas envelope that encloses the accretion disk at the time when accretion just starts. The real column density filtering the BH radiation is time dependent and decreases as accretion proceeds.

Regarding the X-ray radiation, although during most of the accretion process the nearby DCBH only emits hard X-ray photons that negligibly influence the H_2 formation, the collective X-ray emission[6] from distant DCBHs and galaxies builds up a high-z X-ray background (XRB) that ionizes the gas and may promote H_2 formation. We also investigate the impact of such a high-z XRB on DCBH formation.

An external radiation field is not the only factor that can suppress H_2 formation and lead to the formation of a DCBH. Inayoshi & Omukai (2012) pointed out that in a protogalaxy, the cold and dense accretion inflows collide with each other near the center and the shocked gas then forms a hot and dense core, where H_2 formation would be suppressed due to collisional dissociation. However, Visbal et al. (2014b) argued that the density required for this scenario to occur is unable to be achieved in a realistic halo. Inayoshi et al. (2015), however, proposed that the high density could be achieved by collision between two protogalaxies with a high relative velocity. On the other hand, Mayer et al. (2010) proposed that when two halos merge, a massive and unstable disk could be produced by merger-driven inflows. A central core forms from this disk by accretion with a high rate ($\gtrsim 10^4\,\dot{M}_\odot\,{\rm yr}^{-1}$), regardless of whether the gas is pristine or enriched. Finally, a DCBH forms in the core. This was questioned by Ferrara et al. (2013), who claimed that if a more realistic equation of state is adopted, then the disk may cool quickly and the accretion rate will drop, leading to a black hole with final mass $\lesssim 100\,M_\odot$. However, a more advanced model has already been investigated by Mayer et al. (2015), and it is found that it is still feasible to form a DCBH via halo merger. In this paper, we only investigate DCBH formation triggered by an external radiation field.

The layout of this paper is as follows. In Section 2 we introduce the one-zone model and the DCBH SEDs. In Section 3 we present the results, including tests of our code for a pure blackbody spectrum and for a normal star-forming galaxy spectrum, and the critical field intensities for DCBH SEDs and their variance when the XRB is considered. We give the conclusions and discussions in Section 4. In Appendix A we compare the optical depth of the DCBH-forming gas cloud to the LW radiation, to the H^- detachment radiation, and to the H_2^+ dissociation radiation. In Appendix B we present discussions on the probability of enhanced DCBH formation. In Appendix C we list the chemical reactions (Table 3) and heating/cooling functions (Tables 4 and 5) included in our chemistry network. Throughout the paper, we use the `Planck` cosmology parameters (Planck Collaboration et al. 2016): $\Omega_m = 0.308$, $\Omega_\Lambda = 0.692$, $h = 0.6781$, $\Omega_b = 0.0484$, $n = 0.9677$, and $\sigma_8 = 0.8149$. The transfer function is from Eisenstein & Hu (1998).

2. Methods

2.1. The One-zone Model

The one-zone model developed here describes the evolution of a gas cloud that eventually collapses to form a Pop III star, a galaxy, or a BH. Similar approaches have been successfully applied to a variety of problems (see, e.g., Omukai 2000, 2001; Omukai et al. 2005; Stacy & Bromm 2007; Sugimura et al. 2014; Visbal et al. 2014c; Inayoshi & Tanaka 2015).

2.1.1. Halo Build Up

The formation of a dark matter halo is described by the "top-hat" spherical collapse scenario, in which the dark matter density $\rho_{\rm d}$ evolves as

$$\rho_{\rm d} = \begin{cases} \dfrac{9\pi^2}{2}\left(\dfrac{1+z_{\rm ta}}{1-\cos\theta}\right)^3 \rho_c(\Omega_m - \Omega_b) & z > z_{\rm halt} \\ \dfrac{9\pi^2}{2}(1+z_{\rm ta})^3 \rho_c(\Omega_m - \Omega_b) & z \leqslant z_{\rm halt}, \end{cases} \quad (1)$$

[6] Generally, soft X-ray photons are trapped in the high column density matter and only hard X-ray photons contribute to the XRB. However, as matter is swallowed by the DCBH, the column density decreases, and eventually soft X-ray photons can also escape from the BH (Pacucci et al. 2015a) and contribute to the XRB as well.

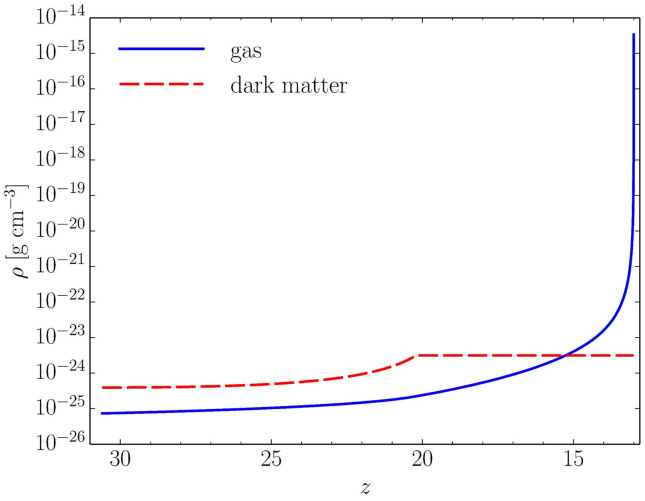

Figure 1. Density evolution of dark matter and collapsing gas cloud in a dark matter halo with turnaround redshift 30.6.

where ρ_c is the universe critical density and $z_{\rm ta}$ is the turnaround redshift; θ is linked to redshift via

$$\theta - \sin\theta = \pi\left(\frac{1+z_{\rm ta}}{1+z}\right)^{3/2}, \quad (2)$$

and by halting the density evolution at the redshift corresponding to $\theta_{\rm halt} = 3\pi/2$, we force the dark matter density to not exceed the final virialization density.[7]

The dark matter halo provides the gravity that causes its gas content to collapse. Ignoring the pressure, the gas density $\rho_{\rm g}$ evolves as

$$\frac{d\rho_{\rm g}}{dt} = \frac{\rho_{\rm g}}{t_{\rm ff}}, \quad (3)$$

where the free-fall timescale

$$t_{\rm ff} = \sqrt{\frac{3\pi}{32G(\rho_{\rm d}+\rho_{\rm g})}}. \quad (4)$$

Throughout this paper, we investigate a halo with $z_{\rm ta} = 30.6$; its gas eventually collapses to form a galaxy or DCBH at $z \sim 13$. In Figure 1 we plot the evolution of the dark matter and gas density, where the initial gas density is set to be $\Omega_b/(\Omega_m - \Omega_b)\rho_{\rm d}(z_{\rm ta})$. This dark matter collapse gets halted at $z \sim 20.5$, and the gas density exceeds the dark matter density at $z \sim 15$.

2.1.2. Temperature Evolution

The temperature of the cloud is followed by solving the energy equation

$$\frac{1}{T}\frac{dT}{dt} = (\gamma-1)\frac{1}{\rho_{\rm g}}\frac{d\rho_{\rm g}}{dt} + \frac{1}{\mu}\frac{d\mu}{dt} + (\gamma-1)\frac{\mathcal{H}-\Lambda}{nk_{\rm B}T}, \quad (5)$$

where $\gamma = 5/3$ is the adiabatic index for the monatomic gas, $k_{\rm B}$ is the Boltzmann constant, μ is the molecular weight, and $n = \rho_{\rm g}/\mu$ is the sum of the number density of all eight species; $\mathcal{H}$ and Λ are the heating and cooling rates per unit volume, respectively.

Even in the pre-reionization epoch, X-ray photons can propagate over long distances and heat the gas with a rate

$$\mathcal{H}_{\rm X} = f_{\mathcal{H}}\mathcal{E}, \quad (6)$$

where $\mathcal{E}$ is the energy (per unit time and volume) of primary electrons due to X-ray ionization, while $f_{\mathcal{H}}$ is the fraction of the primary energy deposited as thermal energy, and we use the value by Valdés & Ferrara (2008; see Shull & van Steenberg 1985 as well). The primary electron energy (here we ignore the photoionization of He^+)

$$\mathcal{E} = \int_{0.1{\rm keV}} dE \frac{4\pi J_X(E)e^{-\tau_{\rm cl}(E)}}{E} \sum_{i={\rm H,He}}(E-E_i)\sigma_i(E)n_i, \quad (7)$$

where J_X is the specific intensity of the XRB (see Section 3.3), and $E_{\rm H} = 13.6\,{\rm eV}$ and $E_{\rm He} = 24.6\,{\rm eV}$ are the ionization potentials for H and He, respectively. The photoelectric cross-sections, $\sigma_{\rm H}(E)$ and $\sigma_{\rm He}(E)$, are from Balucinska-Church & McCammon (1992). The optical depth of the gas cloud is given as

$$\tau_{\rm cl}(E) = \sum_{i={\rm H,He}}\sigma_i(E)n_i\lambda_J/2, \quad (8)$$

using the cloud Jeans length λ_J.

In addition to the X-ray heating, we also take into account the heating associated with the chemical reactions listed in Table 4 in Appendix C. However, throughout this paper, we are concerned with DCBH formation in the pre-reionization epoch, when the neutral IGM is opaque to UV photons, hence we ignore the ionization and heating by these photons.

We stop our calculations at $n \sim 10^9\,{\rm cm}^{-3}$, because our treatment of H_2 cooling is only valid for number densities $\lesssim 10^9\,{\rm cm}^{-3}$, when the gas is optically thin to H_2 lines (e.g., Yoshida et al. 2006). However, according to some previous works (e.g., Omukai 2001) that investigated the subsequent evolution up to density $\gg 10^9\,{\rm cm}^{-3}$, we can conclude that as long as the H_2 formation has been suppressed in the cloud before the density reaches $\sim 10^4\,{\rm cm}^{-3}$, H_2 is collisionally dissociated in higher density, and the cloud continues to collapse only via atomic cooling. This will result in the formation of a supermassive star at the center, which will then collapse to a BH (Umeda et al. 2016).

2.2. Chemical Reactions

We consider the evolution of eight chemical species H^-, H, H^+, H_2, H_2^+, He, He^+, and e^- (we ignore He^{++} since it plays a negligible role) using the reaction rates listed in Table 3 in Appendix C. The reaction rates are collected from Palla et al. (1983), Omukai (2000), Glover & Abel (2008), and Shang et al. (2010), and the original references are found in these works. In a cloud irradiated by an external radiation field, H_2 formation is suppressed via the following three reactions: H_2 photodissociation,

$$H_2 + \gamma \xrightarrow{k_{\rm H_2,dis}} 2H, \quad (9)$$

[7] In the literature, in the top-hat spherical collapse scenario, usually the "virialization redshift" refers to the "collapse redshift," i.e., the redshift corresponding to $\theta_{\rm vir} = 2\pi$ when the density approaches infinity. However, this singularity does not happen in practice, since the gas collapse gets halted well before it.

H^- photodetachment,

$$H^- + \gamma \xrightarrow{k_{H^-,det}} H + e^-, \quad (10)$$

and H_2^+ photodissociation,

$$H_2^+ + \gamma \xrightarrow{k_{H_2^+,dis}} H + H^+, \quad (11)$$

where $k_{H_2,dis}$, $k_{H^-,det}$, and $k_{H_2^+,dis}$ are the corresponding reaction rates (i.e., k_{22}, k_{23}, and k_{24} in Table 3). The photodissociation and photodetachment rates of H_2, H^-, and H_2^+ are described below in Sections 2.2.1, 2.2.2, and 2.2.3, respectively. We only consider the photoionization by the XRB (Section 2.2.4), and ignore all reactions that need ionizing photons other than X-rays.

2.2.1. Photodissociation of H_2

Photons in the narrow LW band can dissociate H_2 through the two-step Solomon process (e.g., Stecher & Williams 1967). The ground electronic state H_2 $X(v'' = 0, J'')$ are excited either to the state $B(v', J')$ by absorbing photons in the Lyman band, or to the state $C(v', J')$ by absorbing photons in the Werner band. A fraction of these excited molecules decay to high ($v'' \geqslant 14$) vibrational levels and then dissociate into separate atoms. The photodissociation rate is then (Abel et al. 1997)

$$k_{H_2,dis} = \sum \frac{\pi e^2}{m_e c} p_{i'} f_{i'} \int \frac{4\pi J(\nu)}{h\nu} \phi_{i'}(\nu - \nu_{i'}) d\nu, \quad (12)$$

where $J(\nu)$ is the specific intensity of the external radiation field at frequency ν, $p_{i'}$ the probability of the transition from the ground state to $B(v', J')$ or $C(v', J')$ (Abgrall & Roueff 1989), $f_{i'}$ the dissociation fraction (Abgrall et al. 1992), $\nu_{i'}$ the frequency of the transition emission line, which has the normalized profile $\phi_{i'}(\nu - \nu_{i'})$, and $\pi e^2/(m_e c) = 2.65 \times 10^{-2}\,cm^2$. We assume that the ground-state hydrogen molecules are para-H_2 with $J'' = 0$ (Abel et al. 1997). In the case where the line profile is a Dirac δ function, the above equation reduces to

$$k_{H_2,dis} \approx \sum \frac{\pi e^2}{m_e c} p_{i'} f_{i'} \frac{4\pi J(\nu_{i'})}{h\nu_{i'}}. \quad (13)$$

The sum is performed for all possible transitions with transition energy smaller than 13.6 eV.

For a blackbody radiation field with effective temperature 10^4 K ("BB") and with mean specific intensity $J_{LW} \times 10^{-21}\,erg\,s^{-1}\,cm^{-2}\,Hz^{-1}\,sr^{-1}$ in the LW band,[8] we have

$$k_{H_2,dis}^{BB} = 7.74 \times 10^{-13} J_{LW} f_{sh} \ (s^{-1}), \quad (14)$$

where the self-shielding effect is included in the self-shielding parameter (Wolcott-Green et al. 2011):

$$f_{sh} = \frac{0.965}{(1 + x/b_5)^{1.1}} + \frac{0.035}{(1+x)^{0.5}} \exp[-8.5 \times 10^{-4}(1+x)^{0.5}], \quad (15)$$

where $x = N_{H_2}/5 \times 10^{14}\,cm^{-2}$ is the H_2 column number density N_{H_2} in units of $5 \times 10^{14}\,cm^{-2}$, and b_5 is the Doppler broadening parameter in units of 10^5 cm s^{-1},

$$b_5 = \frac{\sqrt{2k_B T/m_{H_2}}}{10^5 \ cm \ s^{-1}}, \quad (16)$$

and m_{H_2} is the hydrogen molecule mass. We ignore the microturbulent velocity; therefore, the self-shielding effect is possibly overestimated here (Glover & Brand 2001). The H_2 column density is given by $N_{H_2} = n_{H_2}\lambda_J/2$, where λ_J is the Jeans length of the gas cloud.

For a star-forming galaxy spectrum ("GAL") with mean LW specific intensity J_{LW},

$$k_{H_2,dis}^{GAL} = 1.23 \times 10^{-12} J_{LW} f_{sh} \ (s^{-1}). \quad (17)$$

Here, we take the star-forming galaxy spectrum from STARBURST99[9] (Leitherer et al. 1999, 2010; Vázquez & Leitherer 2005) and adopt the continuous star formation mode, Salpeter initial mass function (IMF) with mass range of 0.1–100 $M_\odot$, metallicity of 0.02 $Z_\odot$, and age of 100 Myr.

For a Compton-thick DCBH, most photons in the UV to soft X-ray bands are absorbed by the thick envelope enclosing the accretion disk, and then re-emitted at energies below 13.6 eV in the form of Lyα emission, two-photon emission, and free–free and free–bound emission, respectively. Therefore, its SED has two main components: the remaining unabsorbed photons (hard X-rays and the <13.6 eV part of the multicolor blackbody radiation) and the re-processed photons. The relative weight of these two components depends on the column number density of the Compton-thick matter.

Using numerical simulations, Pacucci et al. (2015a) carefully investigated the radiation from DCBHs. They obtained the SEDs for different N_H values. In Figure 2 we show the SEDs of Compton-thick DCBHs with $N_H = 1.3 \times 10^{25}\,cm^{-2}$ ("BH1"), $8.0 \times 10^{24}\,cm^{-2}$ ("BH2"), and $5.0 \times 10^{24}\,cm^{-2}$ ("BH3"), 10 Myr after accretion starts. They are for the standard disk, LDP density profiles (the density profile after a BH has already formed at the center) with different normalizations; see Pacucci et al. (2015a) for details. We only plot the energy range relevant to the H_2 chemistry, ignoring the >13.6 eV part. For all three SEDs, the two-photon emission is the dominant radiation from ~3 eV to ~11.2 eV; below ~3 eV, the free–bound emission dominates over the others. The higher the N_H, the more energy is re-processed to the <13.6 eV part, and such an SED is expected to suppress H_2 formation more efficiently. In the case where the envelope is rather thick, i.e., $N_H \gtrsim 10^{25}\,cm^{-2}$, Ly$\alpha$ emission is barely seen, as the corresponding photons are well-trapped in the thick envelope and finally, most of them escape from the envelope as two-photon emission.

[8] Note that in the literature, the radiation field strength is sometimes represented by different quantities. For example, Abel et al. (1997) used the specific intensity at 12.87 eV, while Shang et al. (2010) used the specific intensity at 13.6 eV. We use the *mean* LW specific intensity instead of the specific intensity at a given energy because our DCBH SEDs are not flat in the LW band and because of the presence of several emission lines in this band.

[9] http://www.stsci.edu/science/starburst99/docs/default.htm

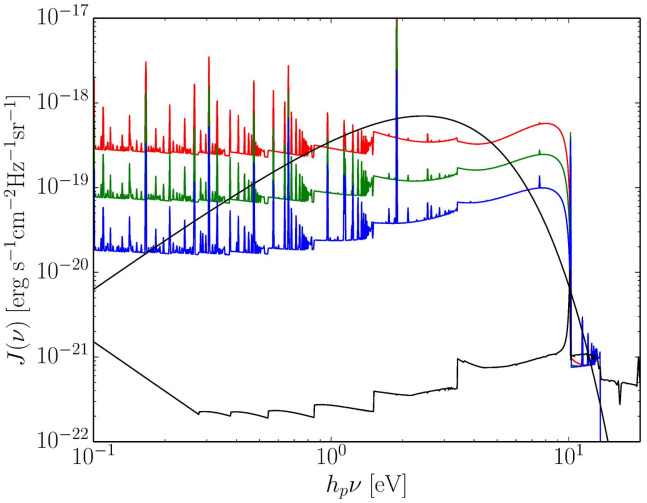

Figure 2. DCBH SEDs (from top to bottom, the three curves with emission lines correspond to BH1, BH2, and BH3, respectively) compared with a blackbody spectrum with effective temperature 10^4 K (smooth curves) and a star-forming galaxy spectrum (bottom curve with sawteeth).

The SED obtained in Pacucci et al. (2015a) evolves as accretion progresses. However, for the BH mass investigated in this paper, the SED is always stationary when the accretion time is smaller than ∼100 Myr; only the normalization changes with increasing BH mass. In our work, we always use the SEDs plotted in Figure 2 as the spectrum of the external radiation field, leaving the normalization as a free parameter representing the different distances from the collapsing gas cloud to the nearby emitting DCBH.

For comparison, the BB and GAL spectra are also shown in Figure 2. All SEDs there have $J_{\rm LW} = 1.0$. Substituting the DCBH SEDs into Equation (13), we find that all three DCBH models have almost the same H_2 photodissociation rate:

$$k_{\rm H_2,dis}^{\rm BH} = 1.30 \times 10^{-12} J_{\rm LW} f_{\rm sh} \ \ ({\rm s}^{-1}). \tag{18}$$

2.2.2. Photodetachment of H^-

H^- could be detached by photons in the wide energy range of 0.755–13.6 eV. The reaction rate is obtained through integration,

$$k_{\rm H^-,det} = \int_{\nu_{0.755}}^{\nu_{13.6}} \frac{4\pi J(\nu)}{h\nu} \sigma_{\rm H^-,det}(\nu) d\nu, \tag{19}$$

where the cross-section is (Abel et al. 1997)

$$\sigma_{\rm H^-,det}(\nu) = 7.928 \times 10^5 (\nu - \nu_{0.755})^{1.5}/\nu^3 \ \ ({\rm cm}^2); \tag{20}$$

$\nu_{0.755}$ is the frequency (in Hz) of a photon with energy 0.755 eV and $\nu_{13.6}$ with 13.6 eV. For the BB and GAL radiation fields with mean LW specific intensity $J_{\rm LW}$, we obtain[10]

$$k_{\rm H^-,det}^{\rm BB} = 5.60 \times 10^{-8} J_{\rm LW} \ \ ({\rm s}^{-1}) \tag{21}$$

and

$$k_{\rm H^-,det}^{\rm GAL} = 5.43 \times 10^{-11} J_{\rm LW} \ \ ({\rm s}^{-1}). \tag{22}$$

[10] Here the mean LW specific intensity, $J_{\rm LW}$, is only used to denote the normalization of the SED; actually all photons with energy $\gtrsim$0.755 eV detach H^-.

For DCBH SEDs,

$$\begin{aligned} k_{\rm H^-,det}^{\rm BH1} &= 5.27 \times 10^{-8} J_{\rm LW} \ ({\rm s}^{-1}) \\ k_{\rm H^-,det}^{\rm BH2} &= 1.87 \times 10^{-8} J_{\rm LW} \ \ ({\rm s}^{-1}) \\ k_{\rm H^-,det}^{\rm BH3} &= 6.29 \times 10^{-9} J_{\rm LW} \ \ ({\rm s}^{-1}). \end{aligned} \tag{23}$$

Apparently, $k_{\rm H^-,det}^{\rm BH1} \approx k_{\rm H^-,det}^{\rm BB} \gg k_{\rm H^-,det}^{\rm GAL}$, and since this is the most relevant reaction suppressing H_2 formation, we therefore expect the critical specific intensity, $J_{\rm LW}^{\rm crit}$, for a BH1 radiation field to be comparable to a BB radiation field but it is much smaller than a GAL radiation field.

2.2.3. Photodissociation of H_2^+

Here we present the photodissociation rate of H_2^+. A more careful investigation of the role played by the H_2^+ channel in H_2 formation can be found in Sugimura et al. (2016), who pointed out that this channel is even more important than the H^- channel in the softer radiation field. H_2^+ is dissociated by photons above 2.65 eV. The reaction has a cross-section (Shapiro & Kang 1987) given by

$$\log(\sigma_{\rm H_2^+}) = \begin{cases} -40.97 + 6.03E_\gamma - 0.504E_\gamma^2 + 1.387 \times 10^{-2}E_\gamma^3 \\ \qquad\qquad (2.65 < E_\gamma < 11.27) \\ -30.26 + 2.79E_\gamma - 0.184E_\gamma^2 + 3.535 \times 10^{-3}E_\gamma^3 \\ \qquad\qquad (11.27 < E_\gamma < 21) \end{cases},$$

where E_γ and the cross-section are in units of eV and cm^2, respectively. Similar to Equation (19), we get the reaction rate for the BB and GAL radiation fields:

$$k_{\rm H_2^+,dis}^{\rm BB} = 4.30 \times 10^{-11} J_{\rm LW} \ \ ({\rm s}^{-1}) \tag{24}$$

and

$$k_{\rm H_2^+,dis}^{\rm GAL} = 6.25 \times 10^{-12} J_{\rm LW} \ \ ({\rm s}^{-1}). \tag{25}$$

For DCBH SEDs,

$$\begin{aligned} k_{\rm H_2^+,dis}^{\rm BH1} &= 8.61 \times 10^{-10} J_{\rm LW} \ ({\rm s}^{-1}) \\ k_{\rm H_2^+,dis}^{\rm BH2} &= 3.63 \times 10^{-10} J_{\rm LW} \ \ ({\rm s}^{-1}) \\ k_{\rm H_2^+,dis}^{\rm BH3} &= 1.46 \times 10^{-10} J_{\rm LW} \ \ ({\rm s}^{-1}). \end{aligned} \tag{26}$$

We have confirmed that the gas cloud is always transparent to both H^- detachment radiation and H_2^+ dissociation radiation, and we ignored their shielding effect; see a check in Appendix A.

2.2.4. Photoionization of H and He by X-Rays

The total ionization rate of hydrogen atoms, including photoionization and secondary ionizations, is

$$\mathcal{I}_{\rm H} = \int dE \frac{4\pi J(E) e^{-\tau_{\rm cl}(E)}}{E} \sigma_{\rm H}(E) n_{\rm H} + \frac{f_{\mathcal{I},{\rm H}}\,\mathcal{E}}{E_{\rm H}}, \tag{27}$$

and of the helium atoms, it is

$$\mathcal{I}_{\rm He} = \int dE \frac{4\pi J(E) e^{-\tau_{\rm cl}(E)}}{E} \sigma_{\rm He}(E) n_{\rm He} + \frac{f_{\mathcal{I},{\rm He}}\,\mathcal{E}}{E_{\rm He}}, \tag{28}$$

where $f_{\mathcal{I},\mathrm{H}}$ and $f_{\mathcal{I},\mathrm{He}}$ are the fractions of primary energy deposited into the secondary ionization in hydrogen and helium, respectively, and are from Valdés & Ferrara (2008).

2.2.5. Numerical Approach

The initial temperature is set as the adiabatic temperature of the IGM at z_{ta} (Barkana & Loeb 2001). The initial H_2 fraction, i.e., the ratio of the H_2 number density to the H and H^+ number density, is set to 10^{-6} (Lepp & Shull 1984; Hirata & Padmanabhan 2006); the initial H^+ fraction and He^+ fraction are all set to 10^{-4}, and the initial electron fraction is their sum; the fractions of other species are set to zero.

We solve the differential equations of the chemistry network together with Equations (3) and (5) starting from z_{ta}, to obtain the evolution of the gas density, temperature, and chemical abundances. To guarantee the precision, we force the time step to be the 0.1% of the minimum of all $y_i/(dy_i/dt)$, where dy_i/dt is the derivative of the ith differential equation, excluding $d\mathrm{H}^-/dt$ and $d\mathrm{H}_2^+/dt$ (see below). The reaction rates for the intermediary species, H^- and H_2^+, are much larger than those for the other species. Hence, to reduce the computational time, we always use the equilibrium abundances for H^- and H_2^+ obtained by iteratively solving simultaneously the following equations:

$$\begin{aligned} n_{\mathrm{H}^-}^{\mathrm{eq}} &= (k_7 n_{\mathrm{H}} n_{\mathrm{e}} + k_{12} n_{\mathrm{H}_2} n_{\mathrm{e}})/(k_8 n_{\mathrm{H}} + k_{10} n_{\mathrm{H}_2^+}^{\mathrm{eq}} + k_{11} n_{\mathrm{H}^+} \\ &\quad + k_{17} n_{\mathrm{e}} + k_{18} n_{\mathrm{H}} + k_{19} n_{\mathrm{H}^+} + k_{\mathrm{H}^-,\mathrm{det}}), \\ n_{\mathrm{H}_2^+}^{\mathrm{eq}} &= (k_5 n_{\mathrm{H}} n_{\mathrm{H}^+} + k_{15} n_{\mathrm{H}_2} n_{\mathrm{H}^+} + k_{19} n_{\mathrm{H}^-}^{\mathrm{eq}} n_{\mathrm{H}^+})/(k_6 n_{\mathrm{H}} \\ &\quad + k_9 n_{\mathrm{e}} + k_{10} n_{\mathrm{H}^-}^{\mathrm{eq}} + k_{\mathrm{H}_2^+,\mathrm{dis}}). \end{aligned} \tag{29}$$

The validity of this treatment has been proven in previous works (e.g., Abel et al. 1997; Omukai & Nishi 1998; Bromm et al. 2002; Omukai et al. 2010).

3. Results

3.1. The Critical Intensity for the Blackbody and Galactic Spectra: Tests of the Code

First, we run the code for a collapsing gas cloud irradiated by the BB and the GAL radiation fields as a test. Here we ignore the XRB.

For the BB radiation field with different strengths, the temperature and the H_2 and e^- fractions are plotted in the upper and bottom panels of Figure 3, respectively. In the absence of an external radiation field or when the radiation field is weak (e.g., $J_{\mathrm{LW}} = 1$), the gas cloud cools by H_2 and attains a temperature $\sim$250–300 K at $n \sim 10^3\,\mathrm{cm}^{-3}$, where the H_2 rotational levels reach local thermodynamic equilibrium. At higher densities, the H_2 cooling rate saturates and the temperature increases gradually, reaching $\sim$800 K at $n \sim 10^9\,\mathrm{cm}^{-3}$, consistent with previous studies (Omukai 2001). On the other hand, with a more intense field, i.e., $J_{\mathrm{LW}} = 30$, H_2 formation and cooling are suppressed, and up to $n \sim 10^9\,\mathrm{cm}^{-3}$, the evolution remains quasi-isothermal at $T \gtrsim 6000$ K, set by the atomic-cooling mechanism.

The blackbody spectrum with effective temperature 10^4 K has $J_{\mathrm{LW}}/J_{\nu_{13.6}} = 3.69$. Hence, $J_{\mathrm{LW}}^{\mathrm{crit}} = 30$ is translated into $J_{\nu_{13.6}}^{\mathrm{crit}} = 8$. This is smaller than that found by Shang et al. (2010), $J_{\nu_{13.6}}^{\mathrm{crit}} = 39$. Latif et al. (2014) and Glover (2015) pointed out that Shang et al. (2010) ignored the dissociative tunneling effect term in Martin et al. (1996). As a result, their H_2 collisional dissociation rate is underestimated. Our critical value is even smaller than that of Glover (2015), who obtained $J_{\nu_{13.6}}^{\mathrm{crit}} \approx 17$. We have checked that such a discrepancy is due to the different initial setups. Using the same initial setups, and using $N_{\mathrm{H}_2} = n_{\mathrm{H}_2}\lambda_J$ instead of $N_{\mathrm{H}_2} = n_{\mathrm{H}_2}\lambda_J/2$, we get $J_{\nu_{13.6}}^{\mathrm{crit}} = 16$, very close to Glover (2015). We further test the same initial setups as Inayoshi & Omukai (2011), and consistently get $J_{\nu_{13.6}}^{\mathrm{crit}} = 16$.

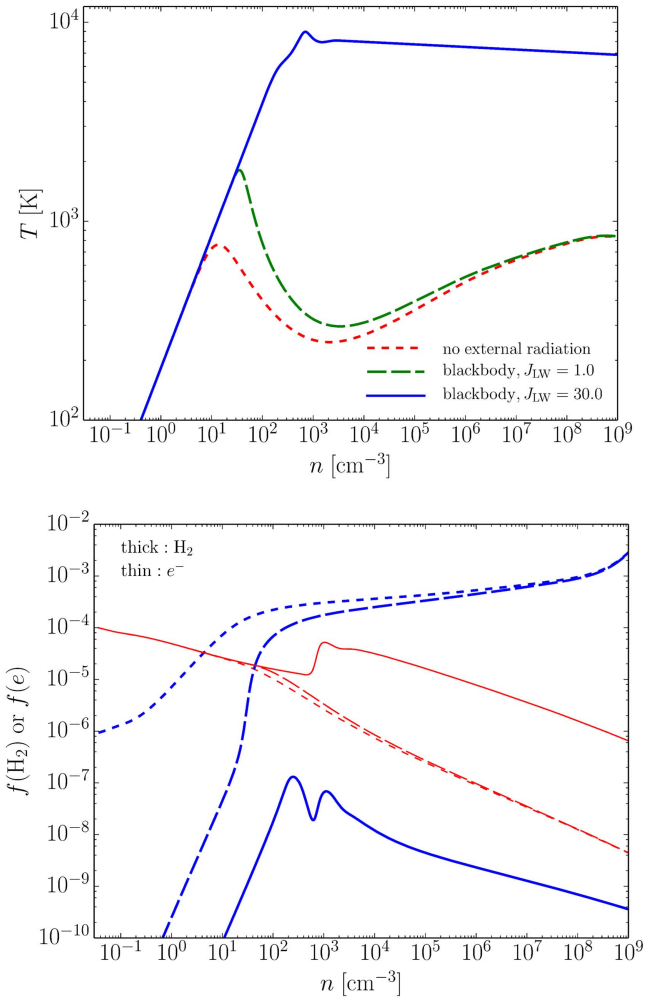

Figure 3. Upper panel: temperature evolution as a function of gas density for a gas cloud irradiated by an external BB radiation field with different J_{LW} values. Bottom: evolution of the H_2 (thick lines) and e^- (thin lines) fractions for the BB model.

In addition to the BB radiation field, we also check the GAL field, and find that when $J_{\mathrm{LW}} \gtrsim 700$, H_2 formation and cooling are suppressed.

The SED of a Compton-thin black hole is composed of two parts with comparable bolometric luminosities (Salvaterra et al. 2005): a multicolor blackbody spectrum that dominates below $\lesssim$0.2 keV, and a power-law spectrum that dominates at $\gtrsim$0.2 keV. The corresponding H_2 photodissociation rate is $\approx 1.26 \times 10^{-12} J_{\mathrm{LW}} f_{\mathrm{sh}}$ (s^{-1}), and the H^- photodetachment rate is $\approx 6.84 \times 10^{-11} J_{\mathrm{LW}}\,\mathrm{s}^{-1}$ and less sensitive to the black hole mass. The rates are similar to a GAL field. We therefore suspect that the critical field strength for a Compton-thin black hole is close to the GAL field. However, in addition to the photons that dissociate H_2 and detach H^-, a Compton-thin

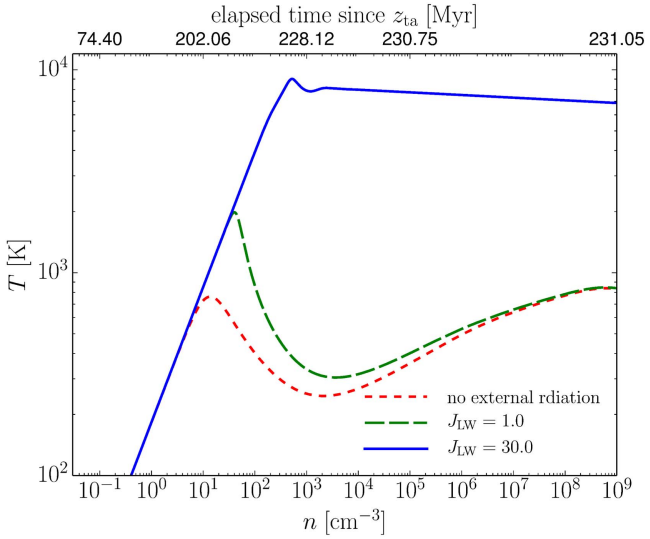

Figure 4. Temperature evolution for the gas cloud irradiated by the BH1 radiation field with different strengths. The model without an external radiation field is also plotted. We mark the time that has elapsed since z_{ta} on the upper x-axis.

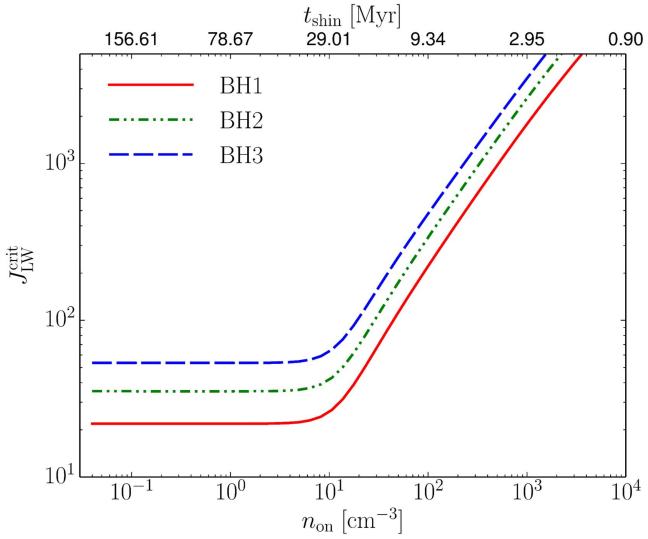

Figure 5. Critical intensity J_{LW}^{crit} vs. the density at which the radiation field is switched on, n_{on}, for different DCBH spectra. The shining time is marked on the upper x-axis.

black hole simultaneously emits lots of UV and soft X-ray photons. These photons ionize and heat the collapsing gas cloud and may either destroy it or enhance the H_2 formation therein (e.g., Regan et al. 2016), resulting in a rather different critical field strength via complex mechanisms. For this reason, we do not investigate such an SED in this test.

3.2. The Critical Intensity by DCBHs: Cases Without XRB

In Figure 4, we show the temperature evolution of a collapsing gas cloud irradiated by the BH1 radiation field for different field strengths, which correspond to different distances to the source DCBH. For this model, we find $J_{LW}^{crit} \approx 22$ and as expected, it is similar to the BB radiation since $k_{H^-,det}^{BB} \approx k_{H^-,det}^{BH1}$. For the BH2 and BH3 spectra, we find $J_{LW}^{crit} \approx 35$ and $J_{LW}^{crit} \approx 54$, respectively.

In the above calculations, the external radiation field is turned on from the initial phase, i.e., $z_{ta} = 30.6$, to the final collapse redshift, i.e., $z_{fin} = 13$. The time interval between these two epochs is ≈233 Myr. This might raise some concerns as such a time span is longer than the typical DCBH accretion time, ∼100 Myr. We note, however, that such a long irradiation time is not really necessary. For most of the time, the gas density and temperature remain around the initial values. Later on, the cumulative H_2 formed during this early evolutionary stages will be easily washed out by the external radiation field as long as it can penetrate into the gas cloud.

We now examine the minimal requirement for the irradiation time. For this purpose, we initially set the external radiation to zero, and switch it on at some gas density n_{on}. We then repeat the calculations for different n_{on} values to obtain the dependence of J_{LW}^{crit} on n_{on}. The result is presented in Figure 5. The shining time t_{shin}, defined as the duration of the irradiation before the final collapse, is also indicated on the upper x-axis. For $n_{on} \lesssim 10\,\mathrm{cm}^{-3}$, J_{LW}^{crit} remains constant, while for higher n_{on}, the increasingly higher J_{LW}^{crit} is needed for the direct collapse. For example, with the BH1 spectrum, for n_{on} as high as $100\,\mathrm{cm}^{-3}$, J_{LW}^{crit} increases to ≈230. In this case, the cloud can be irradiated for only ∼9 Myr (from $n = 100\,\mathrm{cm}^{-3}$ to the final collapse). If the external radiation field is switched on at $n_{on} = 1000\,\mathrm{cm}^{-3}$, the required intensity is even higher, $J_{LW}^{crit} \approx 1800$. In this case, the external radiation field is only required for ∼3 Myr.

Table 1
Fitting Coefficients for the J_{LW}^{crit}–n_{on} Relation

Spectrum	c_1	c_2	c_3	c_4
BH1	1.34	23.3	0.83	−0.60
BH2	1.55	22.3	0.82	−0.60
BH3	1.73	21.8	0.80	−0.60

Table 2
Fitting Coefficients for the J_{LW}^{crit}– t_{shin} Relation

Spectrum	d_1	d_2	d_3	d_4
BH1	1.34	14.6	−1.49	2.65
BH2	1.55	14.5	−1.45	2.59
BH3	1.73	14.5	−1.43	2.53

The J_{LW}^{crit}–n_{on} relation shown in Figure 5 can be fitted by a formula

$$\log(J_{LW}^{crit}) = c_1 + (1 - e^{-n_{on}/c_2})[c_3 \log(n_{on}) + c_4] \quad (30)$$

for each type of the spectrum. The coefficients $c_1 - c_4$ are presented in Table 1. It may be more convenient to know the t_{shin} in some cases; we therefore also fit a formula to the $J_{LW}^{crit} - t_{shin}$ relation,

$$\log(J_{LW}^{crit}) = d_1 + (1 - e^{-d_2/t_{shin}})[d_3 \times \log(t_{shi}) + d_4]; \quad (31)$$

the parameters are listed in Table 2.

3.3. The Impact of an XRB

The XRB ionizes the cloud, producing more free electrons and promoting H_2 formation. As such, it works as a negative feedback on DCBH formation and boosts the critical intensity (Inayoshi & Omukai 2011). Here, we study to what extent the critical intensity is modified by the presence of an XRB. We consider two types of X-ray sources: (i) accreting DCBHs and (ii) first galaxies.

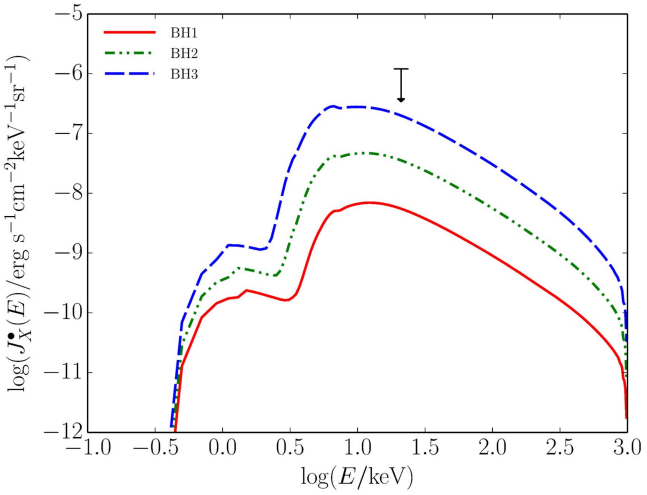

Figure 6. Spectral energy distributions of the XRB from DCBH populations with shielding columns $N_{\rm H} = 1.3 \times 10^{25}$ cm^{-2} ("BH1"), 8.0×10^{24} cm^{-2} ("BH2"), and 5.0×10^{24} cm^{-2} ("BH3") from the bottom to top, respectively, assuming the BH accretion rate density $\dot{\rho}_\bullet = 1 \times 10^{-3}\,M_\odot$ yr^{-1} Mpc^{-3} at $z = 13$. The arrow is the upper limit derived from the present-day observed XRB level at 1.5 keV by Moretti et al. (2012)

3.3.1. X-Rays from DCBHs

Since a DCBH is Compton-thick during most of its accretion stage, soft X-rays are absorbed in the envelope. Only hard X-rays come out from the source, which have a negligible impact on a nearby forming DCBH. However, near the end of accretion, with most of the halo gas reservoir having been swallowed by the growing DCBH, some soft X-ray photons can leak out of the system (Pacucci et al. 2015a). Such soft X-rays from DCBHs cumulatively build up a high-z XRB.

We first derive the XRB spectrum from accreting DCBHs. Assuming that the DCBH formation rate is proportional to the formation rate of atomic-cooling halos with the virial temperature in the range 10,000 K $< T_{\rm vir} <$ 20,000 K, the DCBH X-ray emissivity is given by

$$e_X^{\bullet}(E', z) = \frac{1}{4\pi}\int_z L_X^{\bullet}(E', \Delta t') f_\bullet \frac{d\mathcal{N}_{\rm h}}{dz'} dz', \quad (32)$$

where $\mathcal{N}_{\rm h}$ is the number density of atomic-cooling halos, $f_\bullet$ their fraction harboring DCBHs, and $\Delta t'$ the time interval between redshifts z and z'. We take the time-dependent $L_X^{\bullet}$ of a DCBH with initial mass $2 \times 10^5\,M_\odot$ from Pacucci et al.'s (2015a) numerical simulations. Since we are mainly interested in the XRB spectral shape, its amplitude is left as a free parameter. To express different XRB levels, we vary the parameter $f_\bullet$, which is also related to the accretion rate density by

$$\dot{\rho}_\bullet(z) = \int_z \dot{M}_\bullet(\Delta t') f_\bullet \frac{d\mathcal{N}_{\rm h}}{dz'} dz', \quad (33)$$

where $\dot{M}_\bullet(\Delta t')$ is the accretion rate onto a BH at a time interval $\Delta t'$ after its birth and taken from the numerical simulations in Pacucci et al. (2015a).[11] There are large uncertainties on the accretion rate density $\dot{\rho}_\bullet$, because both the occupation fraction of DCBHs in atomic-cooling halos and the BH mass distribution are not well-known. In the following, we therefore consider $\dot{\rho}_\bullet$ as a free parameter. The specific intensity of XRB at redshift z is then

$$J_X^{\bullet}(E, z) = (1+z)^3 \int_z e_X^{\bullet}(E', z') e^{-\tau_{\rm IGM}(E')} \frac{dr_p}{dz'} dz', \quad (34)$$

where $E' = E(1+z')/(1+z)$, and r_p is the proper distance. The IGM optical depth for X-ray photons is

$$\tau_{\rm IGM}(E') = \int_z^{z'} \left[\sum_{i={\rm H,He}} \bar{n}_i(z'')\sigma_i(E'')\right] \frac{dr_p}{dz''} dz'', \quad (35)$$

where $E'' = E(1+z'')/(1+z)$ and $\bar{n}_i$ is the mean number density of species i in the IGM (the trace-amount metals in the IGM are ignored).

We plot the XRBs at $z = 13$ for the three types of source DCBH spectra in Figure 6 for $\dot{\rho}_\bullet = 10^{-3}\,M_\odot$ yr^{-1} Mpc^{-3}. Based on the fact that the present-day intensity does not fall below the redshifted intensity from the past, i.e.,

$$J_X(E, z=0) \gtrsim (1+z)^{-3} J_X(E(1+z), z), \quad (36)$$

we can put a constraint on the XRB at high redshift from the present-day XRB from unresolved sources, $EJ_X(1.5\ {\rm keV}, z = 0) = 2 \times 10^{-13}$ erg s^{-1} cm^{-2} deg^{-2} (Moretti et al. 2012). The upper limit thus obtained for the XRB at $z = 13$ is $J(21\ {\rm keV}, z = 13) < 1.2 \times 10^{-6}$ erg s^{-1} cm^{-2} keV^{-1}sr^{-1}, which is shown in Figure 6 by a downward arrow.

Armed with the XRB spectrum above, we next investigate the impact of XRB on the DCBH formation. By repeating the temperature evolution calculations for one of the three DCBH spectra (BH1-3 with $N_{\rm H} = 1.3 \times 10^{25}$, 8.0×10^{24}, and 5.0×10^{24} cm^{-2}) with the XRB of the same $N_{\rm H}$, we can derive the critical intensity $J_{\rm LW}^{\rm crit}$ for the DCBH formation as a function of $\dot{\rho}_\bullet$. The result is shown in Figure 7 for the three DCBH spectra. For the same XRB level (i.e., $\dot{\rho}_\bullet$), $J_{\rm LW}^{\rm crit}$ increases with decreasing $N_{\rm H}$, similar to the cases without the XRB. In the case of BH1, $J_{\rm LW}^{\rm crit}$ remains $\approx$22 below $\dot{\rho}_\bullet \sim 10^{-4}\,M_\odot$ yr^{-1} Mpc^{-3}. The behavior of $J_{\rm LW}^{\rm crit}$ is also similar for the BH2(3) cases: $J_{\rm LW}^{\rm crit}$ is always $\approx$35 (54) below $\dot{\rho}_\bullet \sim 10^{-5}(10^{-6})\,M_\odot$ yr^{-1} Mpc^{-3}.

Assuming that active DCBHs accrete at the Eddington-limit rate[12] with radiative efficiency of 0.1, we can translate the accretion rate density $\dot{\rho}_\bullet$ into an *active* BH mass density $\rho_\bullet$:

$$\frac{\rho_\bullet}{M_\odot\ {\rm Mpc^{-3}}} \approx 4.1 \times 10^7 \frac{\dot{\rho}_\bullet}{M_\odot\ {\rm yr^{-1}\ Mpc^{-3}}}. \quad (37)$$

Therefore, the critical active BH mass densities above which the XRB gives negative feedback for the DCBH

[11] Strictly speaking, BHs with different initial masses have different growth histories. Although during their growth $L_X^{\bullet}$ is found to be almost proportional to the BH mass in the Pacucci et al. (2015a) simulations, the final XRB may depend on both the number fraction of BHs in newly formed atomic-cooling halos and the IMF of BHs.

[12] Note, however, that simulations by Pacucci et al. (2015a) show that super-Eddington accretion may occur in highly obscured environments, where radiation trapping is so efficient that photons are advected inward rather than being radiated away; thus, the effect of radiation pressure is dramatically reduced.

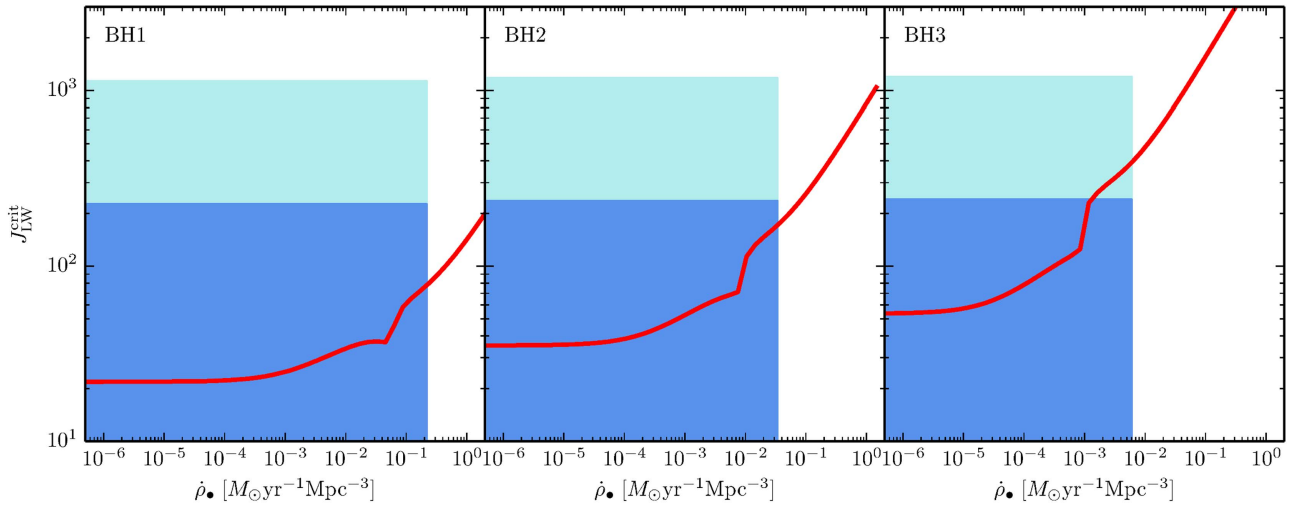

Figure 7. $J_{\rm LW}^{\rm crit}$ as a function of $\dot{\rho}_\bullet$ for the three DCBH models. We fill the regions where the XRB produced by $\dot{\rho}_\bullet$ is below the present-day XRB level constraints, and the required $J_{\rm LW}^{\rm crit}$ can be provided by an emitting DCBH with mass $2 \times 10^5\,M_\odot$ (dark shaded) and $1 \times 10^6\,M_\odot$ (light and dark shaded).

formation are about $4 \times 10^3\,M_\odot$ Mpc^{-3}, $4 \times 10^2\,M_\odot$ Mpc^{-3}, and $4 \times 10^1\,M_\odot$ Mpc^{-3} for the three $N_{\rm H}$ models, respectively.

With an accretion rate density $\dot{\rho}_\bullet$ higher than the above value, the XRB effect becomes noticeable and $J_{\rm LW}^{\rm crit}$ increases with $\dot{\rho}_\bullet$. However, even with $\dot{\rho}_\bullet$ as high as the maximum allowed by the present-day XRB level, the DCBH can still form with a feasible $J_{\rm LW}^{\rm crit}$. For the BH1 model, the maximum allowed accretion rate density is $\approx 0.22\,M_\odot$ yr^{-1} Mpc^{-3}, corresponding to $\rho_\bullet = 9.0 \times 10^6\,M_\odot$ Mpc^{-3}. At this limit, $J_{\rm LW}^{\rm crit}$ only increases to $\approx$80. Under the same hypothesis, for the BH2(3) model at the maximally allowed accretion rate density, $\dot{\rho}_\bullet = 0.034(0.006)\ M_\odot$ yr^{-1} Mpc^{-3}, we get $J_{\rm LW}^{\rm crit} \approx 170$ (390).

All these $J_{\rm LW}^{\rm crit}$ values are still much smaller than those for normal star-forming galaxies, i.e., $\sim$1000–10,000 (Sugimura et al. 2014; Latif et al. 2015; Agarwal et al. 2016b). This indicates that even with the XRB, the DCBHs are efficient radiation sources for triggering DCBHs in nearby halos. Moreover, an accreting BH is usually much brighter than a galaxy, e.g., for a DCBH with mass $10^6\,M_\odot$, the Eddington luminosity is $\approx 1.3 \times 10^{44}$ erg s^{-1}, while a galaxy with our GAL spectrum and star formation rate (SFR) $10\,M_\odot$ yr^{-1} has bolometric luminosity $\approx 3 \times 10^{42}$ erg s^{-1}. Hence, even if $J_{\rm LW}^{\rm crit}$ is the same, BH radiation can exceed $J_{\rm LW}^{\rm crit}$ more easily and can suppress H_2 formation in a larger number of nearby metal-free halos (Yue et al. 2014). Furthermore, if a star-forming galaxy is the dissociation radiation source, it also produces strong soft X-rays, which would counteract the H_2 dissociation (see Section 3.3.2 below). However, it does not happen for the surrounding DCBHs since soft X-ray photons do not leak out from the envelope during the Compton-thick stage ($\sim$100 Myr).

Finally, we evaluate the appropriate distance from a halo that will bear a DCBH ("hatching halo") to the radiation source ("source halo"). If the hatching halo is close enough to the source, the radiation intensity exceeds $J_{\rm LW}^{\rm crit}$ and H_2 formation is suppressed. However, if the distance between them is too small, the hatching halo could be tidally disrupted by the gravity of the source halo. The tidal radius of the hatching halo is defined as (Binney & Tremaine 1987; Chon et al. 2016)

$$r_{\rm TD} = \left(\frac{M_{\rm hat}}{3M_{\rm sou}}\right)^{1/3} d, \tag{38}$$

where $M_{\rm hat}$ and $M_{\rm sou}$ are the masses of the hatching halo and source halo, respectively, and d is the distance between them. The matter of the hatching halo that is outside the tidal radius would be removed by the tidal force.

We conservatively require that for the hatching halo to keep its density without being tidally disrupted, the tidal radius $r_{\rm TD}$ should be larger than the virial radius $r_{\rm vir}$. Assuming $M_{\rm hat} \approx M_{\rm sou}$, we obtain $d > \sqrt[3]{3}\,r_{\rm vir} = 1.44 r_{\rm vir}$. In Figure 7, we indicate the regions where the XRB from DCBHs is well below the present-day XRB constraints, and the required $J_{\rm LW}^{\rm crit}$ can be provided by a source DCBH of 2×10^5 or $1 \times 10^6\,M_\odot$ located at the distance larger than $d > 1.44 r_{\rm vir}$, where $r_{\rm vir}$ is evaluated for $T_{\rm vir} = 10^4$K and $z = 13$. Figure 7 indicates that for any DCBH spectrum considered, there is still a large parameter space for the DCBH formation without being tidally disrupted.

3.3.2. X-Rays from Both the First Galaxies and DCBHs

Next, we also consider the XRB created by the first galaxies $J_X^{\rm gal}$ and add it to that by DCBHs, $J_X^\bullet$.

We assume that the high-mass X-ray binaries (HMXBs) are the sources of the XRB since they contribute the most to the galactic X-ray radiation among three major contributors, i.e., HMXBs, low-mass X-ray binaries, and hot interstellar medium (see, e.g., Pacucci et al. 2014 for details). The X-ray SED of HMXBs follows a power law with index α_X, with its normalization depending on the SFR:

$$L_X^{\rm HMXB}(E) = \frac{(1-\alpha_X) L_{\rm band}({\rm SFR}, z)}{E_2^{(1-\alpha_X)} - E_1^{(1-\alpha_X)}} E^{-\alpha_X}, \tag{39}$$

where $L_{\rm band}$ is the X-ray luminosity in the energy range considered ($E_1 < E < E_2$), and we adopt the spectral index $\alpha_X = 1.5$ in the following. We use the fitting formula for the luminosity in 2–10 keV (below 2 keV, the X-ray photons might be absorbed by the host galaxy gas; therefore, the above

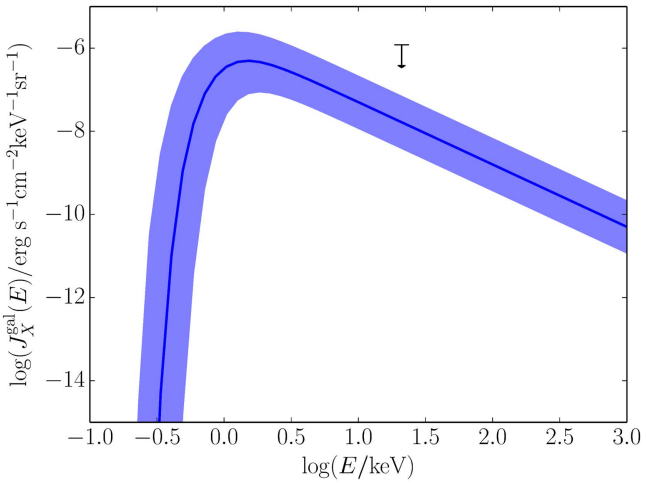

Figure 8. $z = 13$ XRB from first galaxies. Fiducial model with $f_* = 0.022$, $\log N_{\rm H\,I}^{\rm gal} = 22$, and $\log L_{\rm band} = 0.93\log(1+z) + 0.65\log(0.67 \times {\rm SFR}) + 39.80$ is plotted with the solid line. The variance corresponding to $f_* = 0.022^{+0.012}_{-0.008}$, $\log N_{\rm H\,I} = 22^{+0.5}_{-0.5}$, and $\log L_{\rm band} = 0.93\log(1+z) + 0.65\log(0.67 \times {\rm SFR}) + 39.80 \pm 0.5$ is shown by the shaded region.

normalization would be not valid; see Pacucci et al. 2014) by Basu-Zych et al. (2013):

$$\log\left(\frac{L_{\rm band}}{{\rm erg\ s^{-1}}}\right) = 0.97\log(1+z) + 0.65\log\left(0.67\frac{\rm SFR}{M_\odot\ yr^{-1}}\right) + 39.80, \quad (40)$$

and to model the scatter we assume a 0.5 dex variance for this relation. Although the almost linear dependence on redshift, $L_{\rm band} \propto (1+z)^{0.97}$, is obtained from fitting to $z < 4$ samples, we here extrapolate it to galaxies at higher redshifts. We have multiplied the SFR by a factor of 0.67 (Madau & Dickinson 2014), so that here the SFR corresponds to the Salpeter IMF with the mass limits of 0.1 and 100 $M_\odot$ we adopted. At $z = 13$ and SFR $= 1\ M_\odot\ {\rm yr}^{-1}$, Equation (40) gives $\log(L_{\rm band}) = 40.8^{+0.5}_{-0.5}$. Note that this brackets the fiducial value of 40.5 adopted in Furlanetto (2006).

The SFR is assumed to be proportional to the halo mass growth rate:

$${\rm SFR}(M, z) = f_* \frac{\Omega_b}{\Omega_m}\frac{M}{2\Delta t_{\rm SF}(M, z)}, \quad (41)$$

where M is the halo mass, and the star formation timescale, $\Delta t_{\rm SF}$, is the time since the median formation time, which is defined as the time when the halo has collected half of its mass, to the redshift z being considered (Giocoli et al. 2007), and f_* is the star formation efficiency.

The star formation efficiency f_* is calibrated from the observed UV luminosity density $\rho_{\rm UV}$, which is derived from the UV luminosity functions of high-z galaxies. By extrapolating the luminosity function in Bouwens et al. (2015b) down to the absolute UV magnitude -10, Bouwens et al. (2015a) has obtained $\rho_{\rm UV}$ as a function of redshift, and it is $\rho_{\rm UV} = 10^{26.2\pm0.2}\ {\rm erg\ s^{-1}\ Hz^{-1}\ Mpc^{-3}}$ at $z = 10$. By equating this with the sum of contributions from all halos calculated theoretically,

$$\rho_{\rm UV} = \int_{M_{\rm min}} l_{\rm UV}(\Delta t_{\rm SF}){\rm SFR}(M, z)\frac{d\mathcal{N}}{dM}dM, \quad (42)$$

where $M_{\rm min}$ is the minimum halo mass that can form stars and for which we adopt the virial mass of $T_{\rm vir} = 10^4$ K, $d\mathcal{N}/dM$ is the halo mass function (Sheth & Tormen 1999; Sheth et al. 2001), and $l_{\rm UV}$ is the UV (at 1500 Å) luminosity per unit SFR for the continuous star formation mode with Salpeter IMF (0.1–100 $M_\odot$) and metallicity $Z = 0.02\ Z_\odot$ taken from STARBURST99, we then obtain $f_* = 0.022^{+0.012}_{-0.008}$.

The XRB from first galaxies at redshift z can be calculated from

$$J_X^{\rm gal}(E, z) = (1+z)^3 \int_z e_X^{\rm gal}(E', z')e^{-\tau_{\rm IGM}(E')}\frac{dr_{\rm p}}{dz'}dz', \quad (43)$$

where the X-ray emissivity

$$e_X^{\rm gal}(E', z) = \frac{1}{4\pi}\int_{M_{\rm min}} f_{\rm esc,X}(E')L_{\rm X}^{\rm HMXB}(E')\frac{d\mathcal{N}}{dM}dM. \quad (44)$$

The X-ray escape fraction $f_{\rm esc,X}$ depends on the neutral hydrogen, neutral helium, and metal content of the host galaxies,

$$f_{\rm esc,X}(E) = \exp[-(\sigma_{X,1}(E)N_{\rm H\,I}^{\rm gal} + \sigma_{X,2}(E)ZN_{\rm H\,I}^{\rm gal})], \quad (45)$$

where $N_{\rm H\,I}^{\rm gal}$ is the column number density of neutral hydrogen, and $\sigma_{X,1}$ and $\sigma_{X,2}$ the synthesis photoelectric cross-section of neutral hydrogen and helium only, and of metal elements with solar abundance, respectively. Both $\sigma_{X,1}$ and $\sigma_{X,2}$ have been converted to units per hydrogen atom (Balucinska-Church & McCammon 1992).

The neutral hydrogen column density in the first galaxies is largely unknown. Lehmer et al. (2016) provide z-dependent expressions for the X-ray luminosity in both the 0.5–2 keV and 2–10 keV bands. By assuming that the 2–10 keV luminosity approximates the intrinsic one while that of the 0.5–2 keV luminosity is attenuated, and comparing these two, we derive $N_{\rm H\,I}^{\rm gal} \sim 3 \times 10^{21}$–$3 \times 10^{22}\ {\rm cm^{-2}}$ for SFR $\sim 10^{-3}$ –$50\ M_\odot\ {\rm yr^{-1}}$ at $z = 13$. Although such a value should only be considered as an educated guess, we nevertheless assume a fiducial value of $\log N_{\rm H\,I}^{\rm gal} = 22$ with ± 0.5 dex scatter, and use it for all $z \geqslant 13$.

In Figure 8, we show the XRB from the first galaxies at $z = 13$ with the variance. They contribute ~0.3%–6% to the unresolved present-day XRB at 1.5 keV. The total XRB is the sum of $J_X^{\rm gal}$ and the DCBH contribution $J_X^\star$. Recall that the latter is a function of $\dot{\rho}_\star$. For this XRB, we re-calculate $J_{\rm LW}^{\rm crit}$ for each $\dot{\rho}_\star$. The results are plotted in Figure 9. Comparing with the values with only the DCBH XRB, $J_{\rm LW}^{\rm crit}$ is boosted by about factors of 2–20. This indicates that the XRB from first galaxies may have a significant negative influence on the DCBH formation although DCBH formation is still feasible.

3.4. The Number Density of DCBHs

The formation rate of DCBHs is

$$\frac{dn_{\rm DCBH}}{dz} \sim \frac{dn_{\rm cool}}{dz}P_{\rm DCBH}, \quad (46)$$

where $dn_{\rm cool}/dz$ is the formation rate of atomic-cooling halos, $P_{\rm DCBH}$ is the probability that a newly formed atomic-cooling

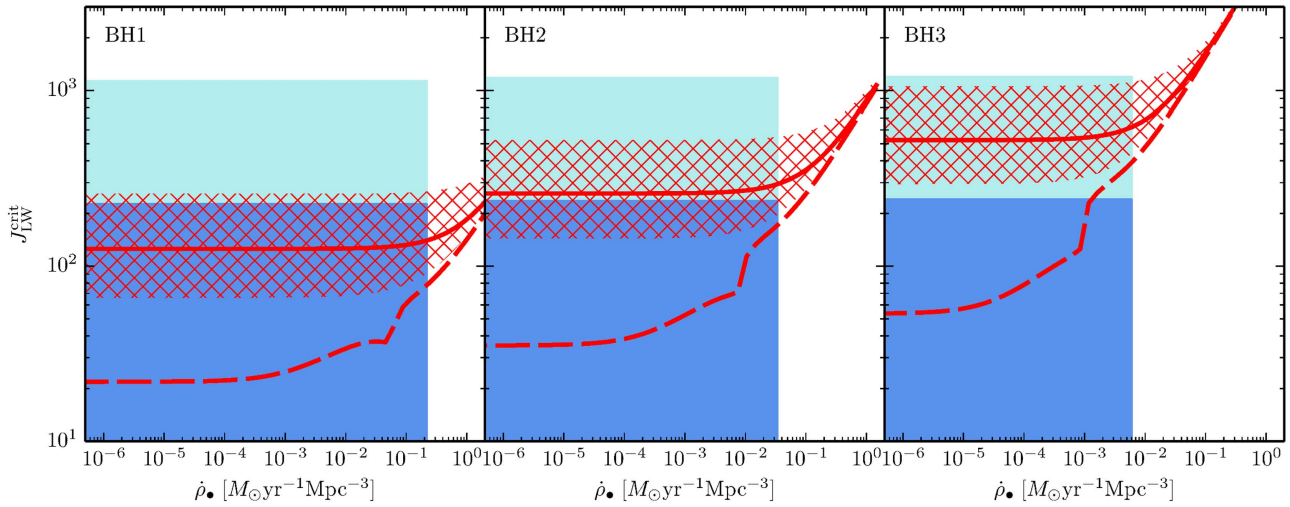

Figure 9. $J_{\rm LW}^{\rm crit}$ against $\dot{\rho}_\bullet$, with the XRB from first galaxies included as well. The shaded regions are allowed space by the present-day XRB constraints and gravitational disruption; see Figure 7. Solid curves correspond to fiducial parameters of first galaxies in Figure 8 while hatched regions are the variance. For reference, we also plot the $J_{\rm LW}^{\rm crit}$ curves in the absence of XRB from first galaxies with the dashed lines.

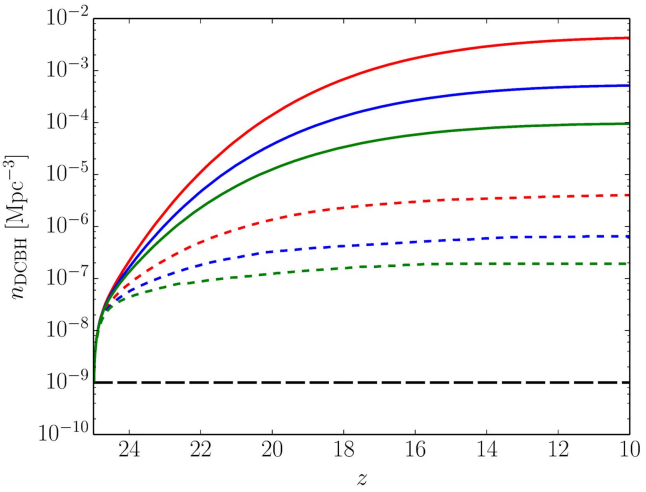

Figure 10. Evolution of the number density of DCBHs when different SEDs and critical field strengths are adopted. Solid (dashed) lines are for the critical field strengths without (with) XRB from first galaxies. From top to bottom, the three solid lines correspond to the BH1 SED with $J_{\rm LW}^{\rm crit} = 22$, BH2 SED with $J_{\rm LW}^{\rm crit} = 35$, and BH3 SED with $J_{\rm LW}^{\rm crit} = 54$. The three dashed lines correspond to the BH1 SED with $J_{\rm LW}^{\rm crit} = 130$, BH2 SED with $J_{\rm LW}^{\rm crit} = 260$, and BH3 SED with $J_{\rm LW}^{\rm crit} = 520$; see Figure 9. The horizontal dashed line refers to the approximate number density of observed SMBHs at $z \gtrsim 6$, $n_{\rm SMBH}(z \gtrsim 6) \sim 10^{-9}$ Mpc^{-3}.

halo matches the DCBH formation criteria. Here we simply assume it to be equal to the probability that this halo is located in a radiation field above the critical threshold. We ignore metal enrichment and radiative feedback (Yue et al. 2014; Johnson et al. 2014). This probability depends on the spatial distribution of the already-formed nearby galaxies and DCBHs. Atomic-cooling halos are assumed to host either star-forming galaxies with SFR as in Equation (41) (here we adopt $f_* = 0.1$) or DCBHs. Using the two-point correlation function that describes the spatial distribution of their host halos, we calculate $P_{\rm DCBH}$ by Monte Carlo simulations, as in Dijkstra et al. (2008, 2014) and Yue et al. (2014).

We solve the Equation (46) from $z = 25$, assuming that the initial number density of DCBHs at this redshift is zero. For simplicity, we assume all DCBHs to have the same luminosity as a $5 \times 10^5\,M_\odot$ black hole.

In Figure 10 we show the evolution of the DCBH number density for different SEDs and critical field strengths. In all models, the final number density of DCBHs is fairly above the observed number density of SMBHs at $z \gtrsim 6$, $n_{\rm SMBH}(z \gtrsim 6) \sim 10^{-9}\,{\rm Mpc}^{-3}$. In some models, $n_{\rm DCBH}$ is even above $\sim \frac{M_{\rm SMBH}}{M_{\rm DCBH}}\, n_{\rm SMBH} \sim \frac{10^9}{10^5} 10^{-9} = 10^{-5}\,{\rm Mpc}^{-3}$. Therefore, DCBHs can act as the original seeds of SMBHs. However, we clarify that there are plenty of factors that can influence the $n_{\rm DCBH}$, for example, the number of DCBHs initially formed by radiation from galaxies, the minimum separation between the collapsing cloud and the triggering source (we adopt 1.44 $r_{\rm vir}$ as discussed[13] in Section 3.3.1), the metal enrichment and radiative feedback (ignored here), and the mass distribution of DCBHs (we assume a fixed mass $5 \times 10^5\,M_\odot$). Therefore, what we present here is not considered a prediction; instead, it is only a proof-of-concept calculation to show how the DCBH number density should be estimated. A conclusive prediction must be based on models that treat the above factors more realistically.

4. Conclusions and Discussion

We have investigated the critical specific intensity of the DCBH radiation that could suppress H_2 formation and cooling in

[13] If the triggering source is a galaxy, the minimum separation must also be larger than the ionized bubble around the galaxy. The ionized bubble radius is estimated by the equilibrium between the ionization rate and the recombination rate,

$$\frac{4\pi}{3} r_{\rm B}^3 n_{\rm H}^2 \alpha_{\rm B} = f_{\rm esc}\,\dot{Q}_{\rm H}, \tag{47}$$

where $n_{\rm H}$ is the mean gas density in the ionized bubble, $\alpha_{\rm B}$ is the recombination coefficient, and $f_{\rm esc}$ and $\dot{Q}_{\rm H}$ are the escape fraction and production rate of the ionizing photons, respectively. From Pallottini et al. (2014), the typical gas density near the galaxy is $\sim$10–$10^{2.5}$ times the mean density of the universe. However, mini halos and dense filaments may boost this factor. Because of the uncertainties on $n_{\rm H}$ and $f_{\rm esc}$, we do not include $r_{\rm B}$ in our calculation in this subsection.

a nearby collapsing gas cloud using one-zone calculations. If the radiation from the emitting DCBH is higher than the critical intensity, we expect that a new DCBH forms in the gas cloud. We used three realistic DCBH SED models from numerical simulations with initial column number densities for the absorbing envelope $N_{\rm H} = 1.3 \times 10^{25}\,{\rm cm}^{-2}$, $N_{\rm H} = 8.0 \times 10^{24}\,{\rm cm}^{-2}$, and $N_{\rm H} = 5.0 \times 10^{24}\,{\rm cm}^{-2}$, respectively.

We have found that:

1. DCBH spectra are very effective at photodetaching H^-, a catalyst species for H_2 formation. Depending on the obscuring gas column density, the ratio between H^- photodetachment and H_2 photodissociation rates for the DCBH with $N_{\rm H} = 1.3 \times 10^{25}\,{\rm cm}^{-2}$ is $k^{\rm BH1}_{\rm H^-,det}/k^{\rm BH1}_{\rm H_2,dis} = 4.1 \times 10^4$, i.e., comparable to that of a blackbody spectrum with effective temperature 10^4 K, which is $k^{\rm BB}_{\rm H^-,det}/k^{\rm BB}_{\rm H_2,dis} = 7.2 \times 10^4$. For the other two DCBH SEDs, $k^{\rm BH2}_{\rm H^-,det}/k^{\rm BH2}_{\rm H_2,dis} = 1.4 \times 10^4$ and $k^{\rm BH3}_{\rm H^-,det}/k^{\rm BH3}_{\rm H_2,dis} = 4.8 \times 10^3$, still much higher than a typical star-forming galaxy, which only yields $k^{\rm GAL}_{\rm H^-,det}/k^{\rm GAL}_{\rm H_2,dis} = 44$.
2. Ignoring the effect of X-rays, the critical field intensity to suppress H_2 formation for the three DCBH SEDs is $J^{\rm crit}_{\rm LW} \approx 22$, 35, and 54, respectively. Note that this is similar to a blackbody radiation field with effective temperature 10^4 K ($J^{\rm crit}_{21} \approx 30$), but much lower than for a typical star-forming galaxy spectrum ($J^{\rm crit}_{\rm LW} \approx 700$). Hence, an emitting DCBH can trigger the formation of a DCBH in a nearby collapsing gas cloud much more efficiently than galaxies.
3. If an XRB produced by previously formed DCBHs is present, it may promote H_2 formation and increase $J^{\rm crit}_{\rm LW}$. For the $N_{\rm H} = 1.3 \times 10^{25}\,{\rm cm}^{-2}$ model, if the accretion rate density is $\dot{\rho}_\bullet \lesssim 10^{-4}\,M_\odot\,{\rm yr}^{-1}\,{\rm Mpc}^{-3}$, the XRB plays a negligible role. However, even if $\dot{\rho}_\bullet$ reaches the maximum value allowed by the present-day XRB level, i.e., $\sim 0.22\,M_\odot\,{\rm yr}^{-1}\,{\rm Mpc}^{-3}$, $J^{\rm crit}_{\rm LW}$ only increases to $\approx$80. For the $N_{\rm H} = 8.0(5.0) \times 10^{24}\,{\rm cm}^{-2}$ SED models, the XRB effect is negligible when $\dot{\rho}_\bullet \lesssim 10^{-5}(10^{-6})\ M_\odot\,{\rm yr}^{-1}\,{\rm Mpc}^{-3}$, and $J^{\rm crit}_{\rm LW}$ increases to $\approx$170(390) at the maximum $\dot{\rho}_\bullet$ allowed by the present-day XRB level, which is $\approx 0.034(0.006)\ M_\odot\,{\rm yr}^{-1}\,{\rm Mpc}^{-3}$. However, if the additional but uncertain XRB contribution from first galaxies is included, it may modify the result by factors in the range $\sim$2–20.

Finally, it is worth noting that several works, for instance Shang et al. (2010) and Latif et al. (2014, 2015), have shown that the $J^{\rm crit}_{\rm LW}$ derived from 3D simulations is almost $\sim$10–100 times higher than from one-zone calculations: "due to the inability of one-zone models to simulate shocks, collapse dynamics and hydrodynamical effects" (Latif et al. 2015, p. 3167). Moreover, they also found that $J^{\rm crit}_{\rm LW}$ varies from halo to halo. Under these circumstances, we might be significantly underestimating $J^{\rm crit}_{\rm LW}$. Further numerical work will be necessary to clarify this point.

B.Y. is supported by the CAS Pioneer Hundred Talents (Young Talents) Program. F.P. acknowledges NASA-ADAP grant MA160009. This work is supported in part by the Grant-in-Aid from the Ministry of Education, Culture, Sports, Science, and Technology (MEXT) of Japan (25287040 KO).

Appendix A
The Optical Depths for H_2, H^-, and H_2^+

Here we check the validity of the optically thin assumption made for H^- detachment radiation and for H_2^+ dissociation radiation. For H^-, the mean optical depth of the gas cloud is

$$\langle \tau_{\rm H^-,det} \rangle = \lambda_J/2 \langle \sigma_{\rm H^-,det} \rangle n_{\rm H^-}, \tag{48}$$

where the mean cross-section is

$$\langle \sigma_{\rm H^-,det} \rangle = k_{\rm H^-,det} \left(\int_{\nu_{0.755}}^{\nu_{13.6}} \frac{4\pi J(\nu)}{h\nu} d\nu \right)^{-1}. \tag{49}$$

This mean cross-section only depends on the spectral shape of the external radiation field; however, it is independent of its strength, which appears in both numerator and denominator. For the BB spectrum, $\langle \sigma_{\rm H^-,det} \rangle = 2.8 \times 10^{-17}\,{\rm cm}^2$. Similarly, we can also calculate the mean cross-section for H_2^+, for which we get $\langle \sigma_{\rm H_2^+,dis} \rangle = 7.0 \times 10^{-19}\,{\rm cm}^{-2}$, and the corresponding mean optical depth $\langle \tau_{\rm H_2^+,dis} \rangle$.

In Figure 11 we plot $\langle \tau_{\rm H^-,det} \rangle$, $\langle \tau_{\rm H_2^+,dis} \rangle$, and $-\log(f_{\rm sh})$ (considered as the mean optical depth to LW radiation) against the n for different external radiation field strengths. This figure shows that since the optical depths to H^- detachment radiation and H_2^+ dissociation radiation are always much smaller, it is then safe to ignore them. On the other hand, even when $J_{\rm LW} \gtrsim J^{\rm crit}_{\rm LW}$, at $n \gtrsim 10^3\,{\rm cm}^{-3}$, the self-shielding effect to LW radiation is not negligible.

Appendix B
Parameter Windows for Enhanced DCBH Formation Probability

In our fiducial model, we adopt the following initial setup: $z_{\rm ta} = 30.6$, adiabatic IGM temperature, ionization fraction 10^{-4}, and H_2 fraction 10^{-6}. In this section, we investigate the influence of alternative initial setups on DCBH formation.

We first check that for the BH1 radiation field, using $z_{\rm ta} = 16$ while keeping other parameters fixed to the fiducial ones, we get $J^{\rm crit}_{\rm LW} \approx 20$. As for the fiducial setup for which we get $J^{\rm crit}_{\rm LW} \approx 22$, we conclude that DCBH formation is insensitive to the cosmic epoch at which the process takes place.

We then take into account the pre-heating of gas by X-rays and shocks before it collapses. In such cases, at $z = z_{\rm ta}$, the gas temperature is higher than the adiabatic IGM temperature. We set the initial gas temperature $T_0 = 30$, 50, 100, and 1000 K, keeping other initial setups the same as our fiducial model, and find that $J^{\rm crit}_{\rm LW}$ increases with increasing T_0: $J^{\rm crit}_{\rm LW} \approx 39$, 49, 50, and 51 for $T_0 = 30$, 50, 100, and 1000 K, respectively. When $T_0 \gtrsim 100$ K, $J^{\rm crit}_{\rm LW}$ almost no longer increases. We conclude that ignoring the gas pre-heating may underestimate the critical field intensity by a factor of at most $\approx$2.

Interestingly, we find that in the model with $T_0 = 30$ K, H_2 formation and cooling could also be suppressed even when the radiation field strength is smaller than $J^{\rm crit}_{\rm LW} \approx 39$, as long as it is in a narrow range, $14.5 \lesssim J_{\rm LW} \lesssim 15.5$, as shown in Figure 12, where we plot the gas temperature at the final step of our calculations ($n \sim 10^9\,{\rm cm}^{-3}$) against $J_{\rm LW}$. To investigate the physics behind this interesting phenomenon, we look through the evolution track and find that when $J_{\rm LW}$ is in this range, the gas almost simultaneously reaches the maximum temperature $\sim 10^4$ K and the critical density for H–H_2 collisional

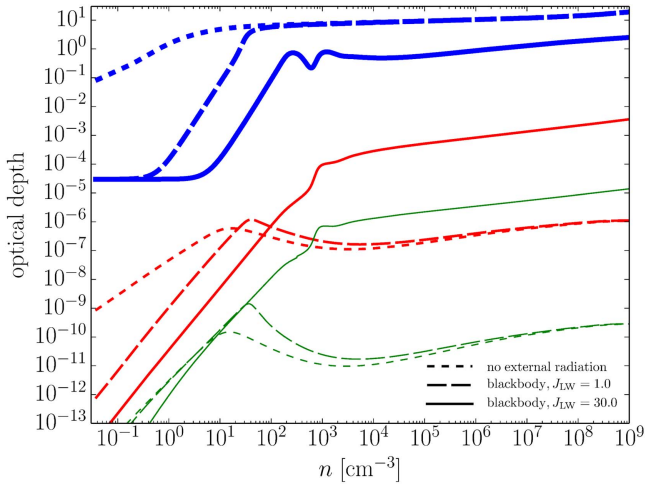

Figure 11. Optical depth against n; thick lines are $-\log(f_{\rm sh})$ for H_2 self-shielding, medium and thin lines are for the H^- and H_2^+, respectively.

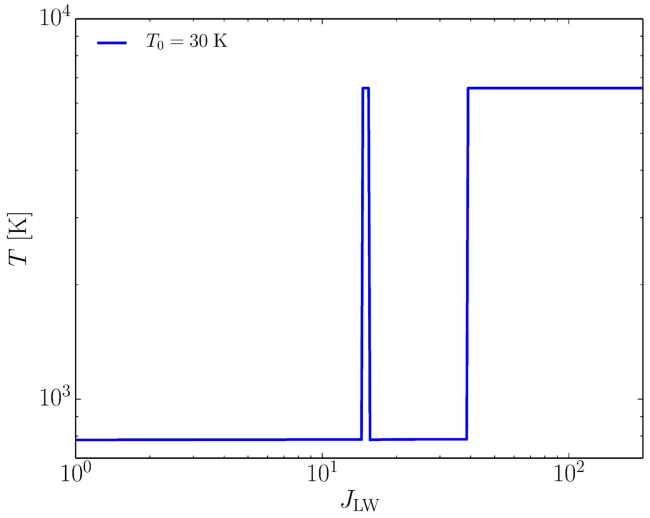

Figure 12. BH1 radiation field. The gas temperature at $n \sim 10^9$ cm^{-3} vs. $J_{\rm LW}$ when the gas has initial temperature $T_0 = 30$ K.

dissociation, $n_{\rm cr,H}$ (see Martin et al. 1996). When the gas number density is higher than $n_{\rm cr,H}$, H_2 is dissociated via the $H_2 + H \xrightarrow{k_{13}} 3H$ reaction with the reaction rate k_{13} approximately proportional to $\exp(-5 \times 10^4/T)$. It has a strong temperature dependence, hence H_2 is dissociated very efficiently at the maximum gas temperature, resulting in suppressed H_2 cooling. If, however, the $J_{\rm LW}$ is smaller than $\sim$14.5, the gas cools earlier and never has a chance to reach the temperature $\sim 10^4$ K, and the collision dissociation is not efficient because of the low temperature, or if the $J_{\rm LW}$ is larger than $\sim$15.5, the radiation reduces (but not fully suppresses) H_2 cooling and the gas temperature reaches 10^4 K before the gas density reaches $n_{\rm cr,H}$. Therefore, H_2 cannot be dissociated efficiently via H–H_2 collisions because of the low density, and the gas temperature decreases early on. The same phenomenon also exists in the $T_0 = 50$ K model, except that the feasible field intensity range is even narrower. However, it does not exist in our fiducial model where $T_0 = 19.8$ K, and the model with $T_0 > 50$ K.

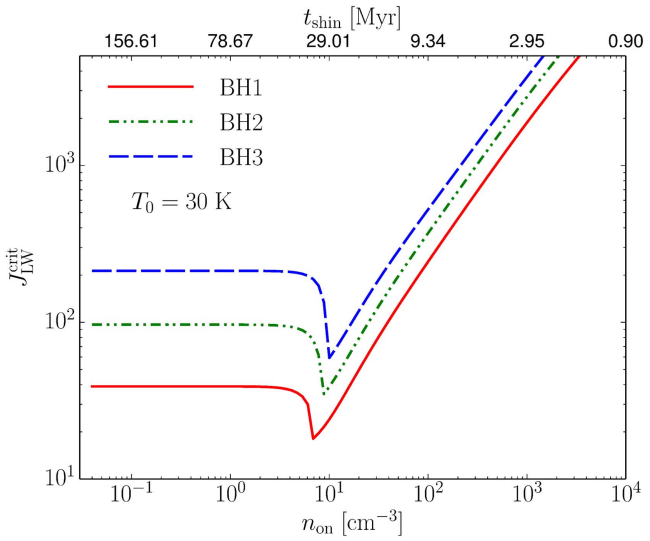

Figure 13. Same as Figure 5; however, $T_0 = 30$ K.

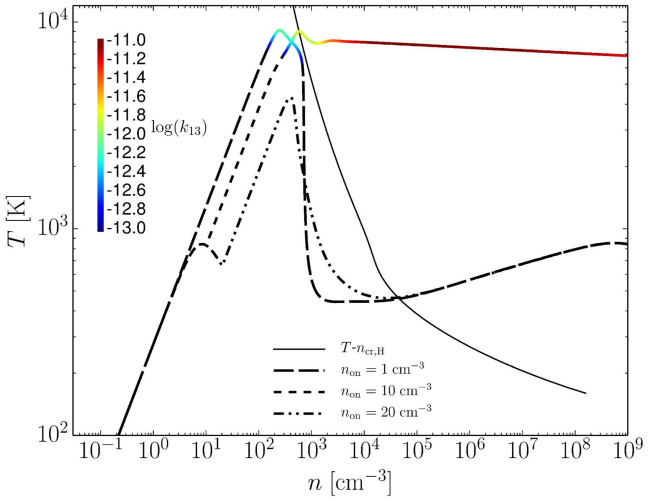

Figure 14. Temperature track if the external BH1 radiation field switched on at total number density 1, 10, and 20 cm^{-3}. In the temperature, we color the segment where the H_2 collisional dissociation rate $k_{13} > 10^{-13}$ cm^3 s^{-1}. In the same panel, we also plot the $T - n_{\rm cr,H}$ curve.

Although the physics mechanism is interesting, the above phenomenon may hardly occur in more realistic cases in which the strength of the external radiation varies with time. However, this mechanism could work in other situations and decrease the critical field intensity; see below.

We re-calculate the $J_{\rm LW}^{\rm crit}$–$n_{\rm on}$ relation for $T_0 = 30$ K; the results are plotted in Figure 13. We find that $J_{\rm LW}^{\rm crit}$ does not increase monotonically with $n_{\rm on}$. Instead, for the BH1 (BH2, BH3) radiation field, when $2\ {\rm cm}^{-3} \lesssim n_{\rm on} \lesssim 15\ {\rm cm}^{-3}$ ($2\ {\rm cm}^{-3} \lesssim n_{\rm on} \lesssim 25\ {\rm cm}^{-3}$, $2\ {\rm cm}^{-3} \lesssim n_{\rm on} \lesssim 35\ {\rm cm}^{-3}$), $J_{\rm LW}^{\rm crit}$ is even smaller than models where the external radiation field irradiates the collapsing gas cloud longer. For example, if the external radiation is switched on at $\sim 7\ {\rm cm}^{-3}$, H_2 suppression is achieved with an intensity as low as $J_{\rm LW}^{\rm crit} \sim 18$ for the BH1 radiation field. We clarify here that $J_{\rm LW}^{\rm crit}$ is not the left boundary of the narrow peak in Figure 12; instead it is the left boundary of the plateau, i.e., for all $J_{\rm LW} \geqslant J_{\rm LW}^{\rm crit}$, H_2 formation and cooling will be suppressed.

Table 3
Rates of Reactions Adopted in this Work

Ordinal	Reaction	Rate[a, b]		Units
(1)	$H + e^- \rightarrow H^+ + 2e^-$	$k_1 = \exp[-32.71396786375 + 13.53655609057(\ln T_{eV}) - 5.739328757388(\ln T_{eV})^2 + 1.563154982022(\ln T_{eV})^3 - 0.2877056004391(\ln T_{eV})^4 + 0.03482559773736999(\ln T_{eV})^5 - 0.00263197617559(\ln T_{eV})^6 + 0.0001119543953861(\ln T_{eV})^7 - 2.039149852002 \times 10^{-6}(\ln T_{eV})^8]$		$cm^3\ s^{-1}$
(2)	$He + e^- \rightarrow He^+ + 2e^-$	$k_2 = \exp[-44.09864886561001 + 23.91596563469(\ln T_{eV}) - 10.75323019821(\ln T_{eV})^2 + 3.058038757198(\ln T_{eV})^3 - 0.5685118909884001(\ln T_{eV})^4 + 0.06795391233790001(\ln T_{eV})^5 - 0.005090561018570001(\ln T_{eV})^6 + 0.0002067236157507(\ln T_{eV})^7 - 3.649161410833 \times 10^{-6}(\ln T_{eV})^8]$		$cm^3\ s^{-1}$
(3)	$H^+ + e^- \rightarrow H + \gamma$	$k_3 = \exp[-28.61303380689232 - 0.7241125657826851(\ln T_{eV}) - 0.02026044731984691(\ln T_{eV})^2 - 0.002380861877349834(\ln T_{eV})^3 - 0.0003212605213188796(\ln T_{eV})^4 - 0.0000142150291405 4107(\ln T_{eV})^5 + 4.989108920299513 \times 10^{-6}(\ln T_{eV})^6 + 5.755614137575758 \times 10^{-7}(\ln T_{eV})^7 - 1.856767039775261 \times 10^{-8}(\ln T_{eV})^8 - 3.071135243196595 \times 10^{-9}(\ln T_{eV})^9]$		$cm^3\ s^{-1}$
(4)	$He^+ + e^- \rightarrow He + \gamma$	$k_4 = 1.54 \times 10^{-9}[1 + 0.3/\exp(8.099328789667/T_{eV})]/[\exp(40.49664394833662/T_{eV}) \times T_{eV}^{1.5}] + 3.92 \times 10^{-13}/T_{eV}^{0.6353}$		$cm^3\ s^{-1}$
(5)	$H + H^+ \rightarrow H_2^+ + \gamma$	$k_5 = 1.85 \times 10^{-23}T^{1.8}$ $k_5 = 5.81 \times 10^{-16}(T/56200)^{[-0.6657\log(T/56200)]}$	$T \leqslant 6.7 \times 10^3$K $T > 6.7 \times 10^3$K	$cm^3\ s^{-1}$
(6)	$H_2^+ + H \rightarrow H_2 + H^+$	$k_6 = 6.0 \times 10^{-10}$		$cm^3\ s^{-1}$
(7)	$H + e^- \rightarrow H^- + \gamma$	$k_7 = 6.775 \times 10^{-15}(T_{eV})^{0.8779}$		$cm^3\ s^{-1}$
(8)	$H + H^- \rightarrow H_2 + e^-$	$k_8 = 1.43 \times 10^{-9}$ $k_8 = \exp[-20.06913897587003 + 0.2289800603272916(\ln T_{eV}) + 0.03599837721023835(\ln T_{eV})^2 - 0.004555120027032095(\ln(T_{eV})^3 - 0.0003105115447124016(\ln(T_{eV})^4 + 0.0001073294010367247(\ln(T_{eV})^5 - 8.36671960467864 \times 10^{-6}(\ln T_{eV})^6 + 2.238306228891639 \times 10^{-7}(\ln(T_{eV})^7]$	$T_{eV} \leqslant 0.1$ $T_{eV} > 0.1$	$cm^3\ s^{-1}$
(9)	$H_2^+ + e^- \rightarrow 2H$	$k_9 = 1 \times 10^{-8}$ $k_9 = 1.32 \times 10^{-6}T^{-0.76}$	$T \leqslant 617$K $T > 617$K	$cm^3\ s^{-1}$
(10)	$H_2^+ + H^- \rightarrow H_2 + H$	$k_{10} = 5 \times 10^{-6}T^{-0.5}$		$cm^3\ s^{-1}$
(11)	$H^- + H^+ \rightarrow 2H$	$k_{11} = 6.5 \times 10^{-9}T_{eV}^{-0.5}$		$cm^3\ s^{-1}$
(12)	$H_2 + e^- \rightarrow H + H^-$	$k_{12} = 2.7 \times 10^{-8}T^{-1.27}\exp(-43000/T)$		$cm^3\ s^{-1}$

Table 3
(Continued)

Ordinal	Reaction	Rate[a, b]		Units
(13)	$H_2 + H \rightarrow 3H$	See Martin et al. (1996)		$cm^3\ s^{-1}$
(14)	$H_2 + H_2 \rightarrow H_2 + 2H$	$k_{14,L} = 1.18 \times 10^{-10} \exp(-6.95 \times 10^4/T)$ $k_{14,H} = 8.125 \times 10^{-8} T^{-1/2} \exp(-5.2 \times 10^4/T)[1 - \exp(-6 \times 10^3/T)]$ $\log n_{cr,H_2} = 4.845 - 1.3 \log(T/10^4) + 1.62[\log(T/10^4)]^2$ $a = (1 + n_H/n_{cr,H_2})^{-1}$, $k_{14} = k_{14,H}^{1-a} k_{14,L}^{a}$		$cm^3\ s^{-1}$
(15)	$H_2 + H^+ \rightarrow H_2^+ + H$	$k_{15} = \exp[-24.24914687731536$ $+3.400824447095291(\ln T_{eV})$ $-3.898003964650152(\ln T_{eV})^2$ $+2.045587822403071(\ln T_{eV})^3$ $-0.5416182856220388(\ln T_{eV})^4$ $+0.0841077503763412(\ln T_{eV})^5$ $-0.007879026154483455(\ln T_{eV})^6$ $+0.0004138398421504563(\ln T_{eV})^7$ $-9.36345888928611 \times 10^{-6}(\ln T_{eV})^8]$		$cm^3\ s^{-1}$
(16)	$H_2 + e^- \rightarrow 2H + e^-$	$5.6 \times 10^{-11} \exp(-102124/T) T^{0.5}$		$cm^3\ s^{-1}$
(17)	$H^- + e^- \rightarrow H + 2e^-$	$k_{17} = \exp[-18.01849334273$ $+2.360852208681(\ln T_{eV})$ $-0.2827443061704(\ln T_{eV})^2$ $+0.01623316639567(\ln T_{eV})^3$ $-0.03365012031362999(\ln T_{eV})^4$ $+0.01178329782711(\ln T_{eV})^5$ $-0.001656194699504(\ln T_{eV})^6$ $+0.0001068275202678(\ln T_{eV})^7$ $-2.631285809207 \times 10^{-6}(\ln T_{eV})^8]$		$cm^3\ s^{-1}$
(18)	$H^- + H \rightarrow 2H + e^-$	$k_{18} = 2.56 \times 10^{-9} T_{eV}^{1.78186}$ $k_{18} = \exp[-20.37260896533324$ $+1.139449335841631(\ln T_{eV})$ $-0.1421013521554148(\ln T_{eV})^2$ $+0.00846445538663(\ln T_{eV})^3$ $-0.0014327641212992(\ln T_{eV})^4$ $+0.0002012250284791(\ln T_{eV})^5$ $+0.0000866396324309(\ln T_{eV})^6$ $-0.00002585009680264(\ln T_{eV})^7$ $+2.4555011970392 \times 10^{-6}(\ln T_{eV})^8$ $-8.06838246118 \times 10^{-8}(\ln T_{eV})^9]$	$T_{eV} \leqslant 0.1$ $T_{eV} > 0.1$	$cm^3\ s^{-1}$
(19)	$H^- + H^+ \rightarrow H_2^+ + e^-$	$k_{19} = 4 \times 10^{-4} T^{-1.4} \exp(-15100/T)$ $k_{19} = 1 \times 10^{-8} T^{-0.4}$	$T \leqslant 10^4$K $T > 10^4$K	$cm^3\ s^{-1}$
(20)	$H + H + H \rightarrow H_2 + H$	$k_{20} = 5.5 \times 10^{-29} T^{-1}$		$cm^6\ s^{-1}$
(21)	$H + H + H_2 \rightarrow H_2 + H_2$	$k_{21} = k_{20}/8$		$cm^6\ s^{-1}$
(22)	$H_2 + \gamma \rightarrow 2H$	See Equations (14), (17), and (18)		s^{-1}
(23)	$H^- + \gamma \rightarrow H + e^-$	See Equations (21), (22), and (23)		s^{-1}
(24)	$H_2^+ + \gamma \rightarrow H + H^+$	See Equations (24), (25), and (26)		s^{-1}

Notes.
[a] T_{eV} and T are the temperature in units of eV and K, respectively.
[b] Reaction (12) is from Glover & Abel (2008); reaction (14) is from Omukai (2000); reactions (20) and (21) are from Palla et al. (1983); all others are from Shang et al. (2010). The original references are found in these cited papers.

Table 4
Heating Functions Used in This Work

Oridinal	Processes	Heating functions[a] (erg cm^{-3} s^{-1})
(1)[b]	two-body H_2 formation	$\mathcal{H}_{2b} = 1.6 \times 10^{-12}\{k_8 n_{H^-} n_H [3.53(1 + n_{cr}/n_H)^{-1}] + k_6 n_{H_2^+} n_H [1.83(1 + n_{cr}/n_H)^{-1}]\}$
(2)	three-body H_2 formation	$\mathcal{H}_{3b} = 1.6 \times 10^{-12} \times 4.48(k_{20} n_H n_H n_H + k_{21} n_H n_H n_{H_2})$

Notes.
[a] All functions from Yoshida et al. (2006); original references are found therein.
[b] $n_{cr} = 10^6\, T^{-1/2} \left\{1.6 y_H \exp\left[-\left(\frac{400}{T}\right)^2\right] + 1.4 y_{H_2} \exp\left[-\left(\frac{12000}{T+1200}\right)\right]\right\}^{-1}$, and y_H and y_{H_2} are the H and H_2 number fractions, respectively.

Table 5
Cooling Functions Used in this Work

Oridinal	Processes	Cooling functions[a, b] (erg cm^{-3} s^{-1})
(1)	Collisional excitation	$\Lambda_{H_2,n_H\to 0} = \mathrm{dex}[-103.0 + 97.59 \log T - 48.05(\log T)^2 + 10.80(\log T)^3 - 0.9032(\log T)^4] n_H n_{H_2}$
		$\Lambda_{H_2,LTE} = \left\{6.7 \times 10^{-19} \exp\left(-\frac{5.86}{T_3}\right) + 1.6 \times 10^{-18} \exp\left(-\frac{11.7}{T_3}\right) + \frac{9.5 \times 10^{-22} T_3^{3.76}}{1 + 0.12 T_3^{2.1}} \exp\left[-\left(\frac{0.13}{T_3}\right)^3\right] + 3 \times 10^{-24} \exp\left(-\frac{0.51}{T_3}\right)\right\} n_{H_2}$
		$\Lambda_{H_2}^{col\text{-}exc} = \frac{\Lambda_{H_2,LTE}}{(1 + \Lambda_{H_2,LTE}/\Lambda_{H_2,n_H\to 0})}$
(2)	Collisional dissociation	$\Lambda_{H_2}^{col\text{-}dis} = 7.2 \times 10^{-12}(k_{13} n_H + k_{14} n_{H_2}) n_{H_2}$
(3)	Recombination	$\Lambda_H^{rec} = 8.7 \times 10^{-27} T^{0.5} T_3^{-0.2} (1 + T_6^{0.7})^{-1} n_e n_{H^+}$
		$\Lambda_{He}^{rec} = 1.55 \times 10^{-26} T^{0.3647} n_e n_{He^+}$
(4)	Collisional ionization	$\Lambda_H^{col\text{-}ion} = 1.27 \times 10^{-21} T^{1/2} (1 + T_5^{0.5})^{-1} \exp\left(-\frac{157809.1}{T}\right) n_e n_H$
		$\Lambda_{He}^{col\text{-}ion} = 9.38 \times 10^{-22} T^{0.5} (1 + T_5^{0.5})^{-1} \exp\left(-\frac{285335.4}{T}\right) n_e n_{He}$
(5)	Collisional excitation	$\Lambda_H^{col\text{-}exc} = 7.5 \times 10^{-19} (1 + T_5^{0.5})^{-1} \exp\left(-\frac{118348}{T}\right) n_e n_H$
		$\Lambda_{He}^{col\text{-}exc} = 9.1 \times 10^{-27} T^{-0.1687} (1 + T_5^{0.5})^{-1} \exp\left(-\frac{13179}{T}\right) n_e^2 n_{He^+}$
		$\Lambda_{He^+}^{col\text{-}exc} = 5.54 \times 10^{-17} T^{-0.397} (1 + T_5^{0.5})^{-1} \exp\left(-\frac{473638}{T}\right) n_e n_{He^+}$
(6)	Bremsstrahlung	$\Lambda^{Bre} = 1.42 \times 10^{-27} T^{0.5} (n_{H^+} + n_{He^+}) n_e$
(7)	Compton	$\Lambda^{com} = 1.017 \times 10^{-37} T_{CMB}^4 (T - T_{CMB}) n_e$

Notes.
[a] $T_3 = T/10^3$ K, $T_5 = T/10^5$ K, $T_6 = T/10^6$ K.
[b] Function (1) is from Galli & Palla (1998) and Hollenbach & McKee (1979); function (2) is from Glover & Jappsen (2007); functions (3)–(5) are from Maselli et al. (2003); functions (6)–(7) are from Maselli et al. (2003). The original references are found in these cited papers.

The physics of this phenomenon is the same as the above. Given $J_{LW} = 30$, in Figure 14 we plot the the temperature tracks for $n_{on} = (1, 10, 20)\,\mathrm{cm}^{-3}$. We also plot the $T - n_{cr,H}$ curve in the same panel. Note that $J_{LW} = 30$ is smaller than the J_{LW}^{crit} for $n_{on} = 1$ and $20\,\mathrm{cm}^{-3}$, but larger than the J_{LW}^{crit} for $n_{on} = 10\,\mathrm{cm}^{-3}$. As seen from Figure 14, for the $n_{on} = 1\,\mathrm{cm}^{-3}$ and $20\,\mathrm{cm}^{-3}$ cases, the temperature track and the $T - n_{cr,H}$ curve intersect at $T \sim 500$ K. However, for the $n_{on} = 10\,\mathrm{cm}^{-3}$ case, the intersection is near 10,000 K. Recall that at $\gtrsim n_{cr,H}$ the reaction rate k_{13} is approximately proportional to $\exp(-5 \times 10^4/T)$. Hence, only if the temperature track and the $T - n_{cr,H}$ curve intersect at high temperatures can the H_2 be rapidly dissociated by H–H_2 collisions; see the colored segment of each curve where k_{13} is shown. In such a situation, H_2 formation and cooling suppression by a weaker external radiation are possible. Moreover, when $n_{on} \gtrsim 100\,\mathrm{cm}^{-3}$, J_{LW}^{crit} increases rapidly because otherwise the previously formed H_2 has already cooled the gas to a low temperature. We note that from $n \sim 2\,\mathrm{cm}^{-3}$ to $\sim 15\,\mathrm{cm}^{-3}$ only about ~ 35 Myr time elapses. This is still a short timescale opportunity for DCBH to form in a weaker external radiation field.

Appendix C
Reaction Rates and Cooling Functions

Tables 3–5 list the rates of reactions, and heating and cooling functions adopted in this work.

References

Abel, T., Anninos, P., Zhang, Y., & Norman, M. L. 1997, NewA, 2, 181
Abgrall, H., Le Bourlot, J., Pineau Des Forets, G., et al. 1992, A&A, 253, 525
Abgrall, H., & Roueff, E. 1989, A&AS, 79, 313
Agarwal, B., Dalla Vecchia, C., Johnson, J. L., Khochfar, S., & Paardekooper, J.-P. 2014, MNRAS, 443, 648
Agarwal, B., Davis, A. J., Khochfar, S., Natarajan, P., & Dunlop, J. S. 2013, MNRAS, 432, 3438
Agarwal, B., Johnson, J. L., Zackrisson, E., et al. 2016a, MNRAS, 460, 4003
Agarwal, B., Khochfar, S., Johnson, J. L., et al. 2012, MNRAS, 425, 2854
Agarwal, B., Smith, B., Glover, S., Natarajan, P., & Khochfar, S. 2016b, MNRAS, 459, 4209
Alvarez, M. A., Wise, J. H., & Abel, T. 2009, ApJL, 701, L133
Aykutalp, A., Wise, J. H., Spaans, M., & Meijerink, R. 2014, ApJ, 797, 139
Balucinska-Church, M., & McCammon, D. 1992, ApJ, 400, 699
Barkana, R., & Loeb, A. 2001, PhR, 349, 125
Basu-Zych, A. R., Lehmer, B. D., Hornschemeier, A. E., et al. 2013, ApJ, 762, 45
Begelman, M. C. 2010, MNRAS, 402, 673
Begelman, M. C., Rossi, E. M., & Armitage, P. J. 2008, MNRAS, 387, 1649
Begelman, M. C., Volonteri, M., & Rees, M. J. 2006, MNRAS, 370, 289
Binney, J., & Tremaine, S. 1987, Galactic Dynamics (Princeton, NJ: Princeton Univ. Press), 747
Bouwens, R. J., Illingworth, G. D., Oesch, P. A., et al. 2015a, ApJ, 811, 140
Bouwens, R. J., Illingworth, G. D., Oesch, P. A., et al. 2015b, ApJ, 803, 34
Bowler, R. A. A., McLure, R. J., Dunlop, J. S., et al. 2016, arXiv:1609.00727
Bromm, V., Coppi, P. S., & Larson, R. B. 2002, ApJ, 564, 23
Bromm, V., & Loeb, A. 2003, ApJ, 596, 34
Choi, J.-H., Shlosman, I., & Begelman, M. C. 2015, MNRAS, 450, 4411
Chon, S., Hirano, S., Hosokawa, T., & Yoshida, N. 2016, ApJ, 832, 134
Dijkstra, M., Ferrara, A., & Mesinger, A. 2014, MNRAS, 442, 2036
Dijkstra, M., Haiman, Z., Mesinger, A., & Wyithe, J. S. B. 2008, MNRAS, 391, 1961
Eisenstein, D. J., & Hu, W. 1998, ApJ, 496, 605
Fan, X., Strauss, M. A., Schneider, D. P., et al. 2003, AJ, 125, 1649
Ferrara, A., Haardt, F., & Salvaterra, R. 2013, MNRAS, 434, 2600
Ferrara, A., Salvadori, S., Yue, B., & Schleicher, D. 2014, MNRAS, 443, 2410
Furlanetto, S. R. 2006, MNRAS, 371, 867
Galli, D., & Palla, F. 1998, A&A, 335, 403
Giocoli, C., Moreno, J., Sheth, R. K., & Tormen, G. 2007, MNRAS, 376, 977
Glover, S. C. O. 2015, MNRAS, 451, 2082
Glover, S. C. O. 2016, arXiv:1610.05679
Glover, S. C. O., & Abel, T. 2008, MNRAS, 388, 1627
Glover, S. C. O., & Brand, P. W. J. L. 2001, MNRAS, 321, 385
Glover, S. C. O., & Jappsen, A. 2007, ApJ, 666, 1
Hartwig, T., Latif, M. A., Magg, M., et al. 2016, MNRAS, 462, 2184
Heger, A., Fryer, C. L., Woosley, S. E., Langer, N., & Hartmann, D. H. 2003, ApJ, 591, 288
Hirata, C. M., & Padmanabhan, N. 2006, MNRAS, 372, 1175
Hollenbach, D., & McKee, C. F. 1979, ApJS, 41, 555
Hosokawa, T., Omukai, K., Yoshida, N., & Yorke, H. W. 2011, Sci, 334, 1250
Inayoshi, K., & Omukai, K. 2011, MNRAS, 416, 2748
Inayoshi, K., & Omukai, K. 2012, MNRAS, 422, 2539
Inayoshi, K., Omukai, K., & Tasker, E. 2014, MNRAS, 445, L109
Inayoshi, K., & Tanaka, T. L. 2015, MNRAS, 450, 4350
Inayoshi, K., Visbal, E., & Kashiyama, K. 2015, MNRAS, 453, 1692
Jeon, M., Pawlik, A. H., Greif, T. H., et al. 2012, ApJ, 754, 34
Jiang, L., Fan, X., Vestergaard, M., et al. 2007, AJ, 134, 1150
Johnson, J. L., Whalen, D. J., Agarwal, B., Paardekooper, J.-P., & Khochfar, S. 2014, MNRAS, 445, 686
Johnson, J. L., Whalen, D. J., Li, H., & Holz, D. E. 2013, ApJ, 771, 116
Koushiappas, S. M., Bullock, J. S., & Dekel, A. 2004, MNRAS, 354, 292
Kurk, J. D., Walter, F., Fan, X., et al. 2007, ApJ, 669, 32
Latif, M. A., Bovino, S., Grassi, T., Schleicher, D. R. G., & Spaans, M. 2015, MNRAS, 446, 3163
Latif, M. A., Bovino, S., Van Borm, C., et al. 2014, MNRAS, 443, 1979
Latif, M. A., & Ferrara, A. 2016, PASA, 33, e051
Latif, M. A., Schleicher, D. R. G., & Hartwig, T. 2016, MNRAS, 458, 233
Latif, M. A., Schleicher, D. R. G., Schmidt, W., & Niemeyer, J. 2013a, MNRAS, 433, 1607
Latif, M. A., Schleicher, D. R. G., Schmidt, W., & Niemeyer, J. C. 2013b, MNRAS, 436, 2989
Lehmer, B. D., Basu-Zych, A. R., Mineo, S., et al. 2016, ApJ, 825, 7
Leitherer, C., Ortiz Otálvaro, P. A., Bresolin, F., et al. 2010, ApJS, 189, 309
Leitherer, C., Schaerer, D., Goldader, J. D., et al. 1999, ApJS, 123, 3
Lepp, S., & Shull, J. M. 1984, ApJ, 280, 465
Lodato, G., & Natarajan, P. 2006, MNRAS, 371, 1813
Madau, P., & Dickinson, M. 2014, ARA&A, 52, 415
Martin, P. G., Schwarz, D. H., & Mandy, M. E. 1996, ApJ, 461, 265
Maselli, A., Ferrara, A., & Ciardi, B. 2003, MNRAS, 345, 379
Mayer, L., Fiacconi, D., Bonoli, S., et al. 2015, ApJ, 810, 51
Mayer, L., Kazantzidis, S., Escala, A., & Callegari, S. 2010, Natur, 466, 1082
Moretti, A., Vattakunnel, S., Tozzi, P., et al. 2012, A&A, 548, A87
Morganson, E., De Rosa, G., Decarli, R., et al. 2012, AJ, 143, 142
Mortlock, D. J., Warren, S. J., Venemans, B. P., et al. 2011, Natur, 474, 616
Omukai, K. 2000, ApJ, 534, 809
Omukai, K. 2001, ApJ, 546, 635
Omukai, K., Hosokawa, T., & Yoshida, N. 2010, ApJ, 722, 1793
Omukai, K., & Nishi, R. 1998, ApJ, 508, 141
Omukai, K., Tsuribe, T., Schneider, R., & Ferrara, A. 2005, ApJ, 626, 627
Pacucci, F., & Ferrara, A. 2015, MNRAS, 448, 104
Pacucci, F., Ferrara, A., Grazian, A., et al. 2016, MNRAS, 459, 1432
Pacucci, F., Ferrara, A., Volonteri, M., & Dubus, G. 2015a, MNRAS, 454, 3771
Pacucci, F., Mesinger, A., Mineo, S., & Ferrara, A. 2014, MNRAS, 443, 678
Pacucci, F., Pallottini, A., Ferrara, A., & Gallerani, S. 2017, MNRAS, 468, L77
Pacucci, F., Volonteri, M., & Ferrara, A. 2015b, MNRAS, 452, 1922
Palla, F., Salpeter, E. E., & Stahler, S. W. 1983, ApJ, 271, 632
Pallottini, A., Ferrara, A., Pacucci, F., et al. 2015, MNRAS, 453, 2465
Planck Collaboration, Ade, P. A. R., Aghanim, N., et al. 2016, A&A, 594, A13
Pallottini, A., Gallerani, S., & Ferrara, A. 2014, MNRAS, 444, L105
Regan, J. A., & Haehnelt, M. G. 2009, MNRAS, 396, 343
Regan, J. A., Johansson, P. H., & Wise, J. H. 2014, ApJ, 795, 137
Regan, J. A., Johansson, P. H., & Wise, J. H. 2016, MNRAS, 461, 111
Salvaterra, R., Haardt, F., & Ferrara, A. 2005, MNRAS, 362, L50
Shang, C., Bryan, G. L., & Haiman, Z. 2010, MNRAS, 402, 1249
Shapiro, P. R., & Kang, H. 1987, ApJ, 318, 32
Sheth, R. K., Mo, H. J., & Tormen, G. 2001, MNRAS, 323, 1
Sheth, R. K., & Tormen, G. 1999, MNRAS, 308, 119
Shull, J. M., & van Steenberg, M. E. 1985, ApJ, 298, 268
Smidt, J., Wiggins, B. K., & Johnson, J. L. 2016, ApJL, 829, L6
Smith, A., Bromm, V., & Loeb, A. 2016, MNRAS, 460, 3143
Sobral, D., Matthee, J., Darvish, B., et al. 2015, ApJ, 808, 139
Stacy, A., & Bromm, V. 2007, MNRAS, 382, 229
Stecher, T. P., & Williams, D. A. 1967, ApJL, 149, L29
Sugimura, K., Coppola, C. M., Omukai, K., Galli, D., & Palla, F. 2016, MNRAS, 456, 270
Sugimura, K., Omukai, K., & Inoue, A. K. 2014, MNRAS, 445, 544
Tanaka, T., Perna, R., & Haiman, Z. 2012, MNRAS, 425, 2974
Umeda, H., Hosokawa, T., Omukai, K., & Yoshida, N. 2016, ApJL, 830, L34
Valdés, M., & Ferrara, A. 2008, MNRAS, 387, L8
Valiante, R., Schneider, R., Volonteri, M., & Omukai, K. 2016, MNRAS, 457, 3356
Vázquez, G. A., & Leitherer, C. 2005, ApJ, 621, 695
Venemans, B. P., Findlay, J. R., Sutherland, W. J., et al. 2013, ApJ, 779, 24
Visbal, E., Haiman, Z., & Bryan, G. L. 2014a, MNRAS, 445, 1056
Visbal, E., Haiman, Z., & Bryan, G. L. 2014b, MNRAS, 442, L100
Visbal, E., Haiman, Z., Terrazas, B., Bryan, G. L., & Barkana, R. 2014c, MNRAS, 445, 107
Volonteri, M. 2010, A&ARv, 18, 279
Wolcott-Green, J., Haiman, Z., & Bryan, G. L. 2011, MNRAS, 418, 838
Wolcott-Green, J., Haiman, Z., & Bryan, G. L. 2017, MNRAS, arXiv:1609.02142
Wu, X.-B., Wang, F., Fan, X., et al. 2015, Natur, 518, 512
Yoshida, N., Omukai, K., Hernquist, L., & Abel, T. 2006, ApJ, 652, 6
Yue, B., Ferrara, A., Salvaterra, R., Xu, Y., & Chen, X. 2014, MNRAS, 440, 1263